THE VELOCITY DEPENDENCE OF SENSITIZED FLUORESCENCE

By

ROBERT ALAN SANDERS

A DISSERTATION PRESENTED TO THE GRADUATE COUNCIL OF
THE UNIVERSITY OF FLORIDA IN PARTIAL
FULFILLMENT OF THE REQUIREMENTS FOR THE DEGREE OF
DOCTOR OF PHILOSOPHY

UNIVERSITY OF FLORIDA

1975

TABLE OF CONTENTS

THE VELOCITY DEPENDENCE OF SENSITIZED FLUORESCENCE

By

Robert Alan Sanders

August, 1975

Chairman: E. E. Muschlitz, Jr.
Major Department: Chemistry

Measurements have been made of the velocity dependence
of the relative cross sections for the reactions:

$$Ar(^3P_{2,0}) + N_2(X^1\Sigma_g^+) \rightarrow Ar(^1S) + N_2(C^3\Pi_u) \qquad (1)$$

and

$$He(2^1S, 2^3S) + N_2(X^1\Sigma_g^+) \rightarrow He(^1S) + N_2^+(B^2\Sigma_u^+) + e \qquad (2)$$
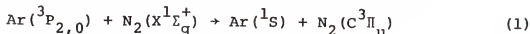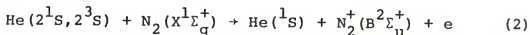
by observation of the fluorescence, $N_2(C \rightarrow B)$ and $N_2^+(B \rightarrow X)$. The
measurements were made in the relative energy ranges 0.06 eV.
to 0.36 eV. for reaction (1) and 0.03 eV. to 0.16 eV. for
reaction (2) using crossed molecular beams. The metastable
atom beams are produced in a low voltage, D.C. discharge and
velocity selected by a mechanical selector of standard
design. The nitrogen beam is a supersonic nozzle beam used
both unseeded and seeded with helium in order to increase
the energy range of the experiments. The nozzle beam is
chopped at 100 hz., the photons are detected by an EMI 9558
photomultiplier with extended red response, and the photon

signal is extracted from background using an SSR dual channel photon counter. The metastable argon atom beam was found to have a $^3P_2/^3P_0$ ratio of 7/1 in an identical source under similar conditions. The metastable helium beam consists predominately of 2^3S states.

The cross section for reaction (1) shows a rapid rise from 0.06 to 0.12 eV., then decreases gradually. The cross section for reaction (2) goes through a minimum at about 0.04 eV., then approximately doubles from 0.04 to 0.10 eV., and continues to rise up to 0.16 eV. The energy dependent cross sections for reaction (2) are compared to total ionization cross sections for the same system, and the branching ratio for the production of $N_2^+(B)$ compared to total ion production is calculated. This ratio decreases rapidly from 0.03 to 0.04 eV., and then, decreases slowly from 0.04 to 0.16 eV.

Reaction (1) is discussed in terms of a curve crossing mechanism. Reaction (2) is discussed in terms of an electron exchange mechanism, and a technique for obtaining theoretical Penning ionization cross section curves for comparison with the experimental curves is presented.

$\overline{\phantom{\rule{8em}{0ex}}}$
Chairman

CHAPTER I

INTRODUCTION

A. Sensitized Fluorescence

Sensitized fluorescence[1] is the process in which electronic energy is transferred from one molecule to another molecule, which subsequently fluoresces. Such electronic energy transfer reactions are relevant to many natural phenomena. For example, a three-step process beginning with the production of electronically excited oxygen atoms has been proposed to explain the intriguing phenomenon of night glow.[2] Energy transfer reactions play an important role in maintaining the delicate balance among the constituents of the earth's atmosphere as well as the atmospheres of other planets and stars. Helium metastable atoms have been suggested as energy carriers in the vast regions of outer space.[3]

In addition to their relevance to various natural phenomena, electronic energy transfer processes have important laboratory applications. These reactions serve as excitation mechanisms in laser systems such as $Ar - O_2$ and $He - Ne$ lasers.[4] Measurements of the dynamic properties of the electronic energy transfer processes involved are invaluable in the design of laser systems for specific purposes. The transfer of electronic excitation energy also offers promise as a synthetic technique to promote reactions which

1

are ordinarily energetically forbidden. For instance, excited oxygen molecules may add directly to double bonds:[5]

$$O_2(a^1 \Delta_g) + H_3C\underset{O}{\overset{O}{\bigsqcup}}CH_3 \rightarrow H_3C\underset{O-O}{\overset{O}{\diagdown}}CH_3.$$
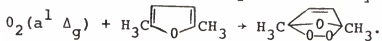
From a puristic viewpoint, studies of energy transfer and other elementary processes have done much to further the understanding of atomic and molecular interactions. The measurements of macroscopic reaction properties may now, to a large extent, be explained in terms of the microscopic interactions between individual atoms and molecules. The realization that these microscopic events must be studied under "single collision" conditions has led to the development of molecular reaction dynamics as a logical extension of physical chemistry. Sensitized fluorescence is just one elementary process being investigated. A survey of the basic principles and experimental techniques for studying microscopic reaction mechanisms is found in the book by Levine and Bernstein.[2]

B. The Study of Electronic Energy Transfer Processes

Electronic energy transfer may occur in several different ways. Depending on whether the electronic excitation energy exceeds the ionization potential of its collision partner, the resulting products may be neutral or ionic. Some of the possible reactions are illustrated below:

A. Neutral Products

$$A^* + XY \rightarrow A + XY^* \tag{1}$$

$$A^* + XY \rightarrow A + X^* + Y \tag{2}$$

B. Ionic Products

$$A^* + XY \rightarrow XY^+ + A + e \tag{3}$$

$$A^* + XY \rightarrow X^+ + Y + A + e \tag{4}$$

$$A^* + XY \rightarrow AXY^+ + e \tag{5}$$

The asterisk denotes an electronically excited species.
In reaction (1) a portion of the electronic energy appears
as electronic (as well as vibrational and rotational)
excitation of XY. In reaction (2) energy transfer is
accompanied by dissociation of XY. Reaction (3) is known
as Penning ionization.[6] Reaction (4) is dissociative
Penning ionization, and reaction (5) is associative
ionization. Whenever an electronically excited atom or
molecule is produced, fluorescence will follow if the
transition is optically allowed.[7]

Sensitized fluorescence was first observed by Cario
and Franck[8] in 1923. Much of the early work has been
reviewed by Willey.[9]

Until recently, the study of electronic energy transfer
processes has been concentrated on the reactions which
yield ionic products--simply because the ionic products
are more readily detected. Several reviews[10-13] summarize
the information known about these processes prior to 1972.
These studies have been designed, primarily, to determine
absolute ionization rate constants or cross sections and/or
the dependence of these cross sections on the relative
velocity of the collision partners. Cross sections for
ionization reactions are intimately related to the interaction

potential of the colliding species, and such measurements
have done much to further the understanding of the Penning
ionization process (see I D). Tang, Marcus, and Muschlitz[14]
studied Penning ionization in the systems Ne($^3P_{2,0}$)/Ar,Kr,Xe
using a neon metastable atom beam and a collision chamber
containing the target gas at a known pressure. By mechan-
ically velocity selecting the metastable atom beam, they
obtained absolute measurements of the total ionization cross
section as a function of the relative velocity in these
systems. Pesnelle et al.[15] has measured the velocity depen-
dence of the Penning ionization cross section for the
He($2^{1,3}S$)/Ar system by a time-of-flight method. Illenberger
and Niehaus[16] have used a crossed beam, time-of-flight method
to measure the velocity dependence of Penning ionization in
the systems He(2^3S) and He(2^1S)/Ar, Kr, Xe, N_2, and Hg;
Ne($^3P_{2,0}$)/Kr, Hg; and Ar($^3P_{2,0}$)/Hg.

Another technique for studying Penning ionization
utilizes the fact that the electron in reactions such as
(3) - (5) carries off most of the excess energy. Thus,
analysis of the energy distribution of the ejected electrons
gives the relative populations of the electronic and vibra-
tional states excited during the collision, as well as
information concerning the shapes of the interaction potential
curves in the transition region. Cermák[17] and Hotop and
Niehaus[18] have employed this method, known as Penning electron
spectroscopy (PES). Comparisions with photoelectron spectra
have shed considerable light on the dynamics of the ioniza-
tion process.

Another powerful technique has been utilized to study both ion producing and non-ion producing reactions. The flowing afterglow (FA) method employs a hollow cathode discharge to produce electronically excited species which then flow into an interaction region where collisional de-excitation occurs. Stedman and Setser[10] have studied reactions either by measuring the decrease in concentration of the electronically excited reactant (as determined from its absorption of radiation from an appropriate light source) or by observation of the fluorescent emission of the excited products produced. The former method allows the determination of total cross sections for quenching of the excited species, while the latter technique allows the determination of relative cross sections for energy transfer into specific rotational, vibrational, and electronic states of the products. This technique has been described in detail by Ferguson, Fehsenfeld, and Schmeltekopf,[19] Bolden et al.[20] and Stedman and Setser.[10]

Three molecular beam techniques have recently been used to study non-ion producing reactions such as (1) and (2). Winicur and Fraites[21] have measured the differential scattering cross section for the system $Ar(^3P_{2,0})/N_2$. From the small angle scattering data (purely elastic) they predicted the elastic scattering at large angles. By subtracting this from the measured cross section, they deduced the inelastic scattering cross section at a particular relative velocity.

Lee and Martin[22] have used a crossed beam, time-of-flight method to measure the velocity dependence of the relative cross section for the reaction:

$$Ar(^3P_{2,0}) + N_2(X \ ^1\Sigma_g^+) \rightarrow Ar(^1S) + N_2(C^3\Pi_u) \tag{6}$$
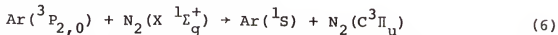
The rate of product formation is followed by detecting photons from the transition $N_2(C) \rightarrow N_2(B)$. In this technique, neither beam is velocity filtered in the usual sense; the velocity selection is accomplished by modulating the metastable atom beam and time resolving the product photon flux. The technique used in the present study is also a crossed beam technique in which the product formation is detected by its photon emission. However, both beams are velocity selected. The metastable atom beam, $He(2^{3,1}S)$ or $Ar(^3P_{2,0})$, is mechanically velocity selected; the target beam, $N_2(X^1\Sigma_g^+)$, is a supersonic nozzle beam which has a narrow velocity distribution and whose nominal velocity is varied by a seeding technique. The relative cross sections for electronic energy transfer as a function of the relative translational energies were measured for reaction (6) and for the following reaction:

$$He(2^{3,1}S) + N_2(X \ ^1\Sigma_g^+) \rightarrow He(^1S) + N_2^+ \ (B \ ^2\Sigma_u^+) + e \tag{7}$$
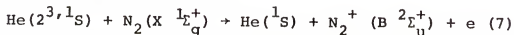
A detailed description of this experimental technique is given in Chapter II.

C. Cross Sections and Rate Constants

For two interacting beams, A and B, the reaction rate, R, at a particular relative velocity is

$$R = \sigma(v_r) v_r \iiint\limits_{x,y,z} n_A(x,y,z) \; n_B(x,y,z) \; \frac{dxdydz}{V} \qquad (8)$$

where v_r is the relative velocity of A with respect to B,
$\sigma(v_r)$ is the reaction cross section, n_A and n_B are the
spatially dependent densities of the interacting molecules
in the volume element $dxdydz$, and V is the volume of the
interaction zone. Experimentally, it is very difficult to
measure absolute density profiles in the intersection
region of crossed molecular beams. It is also difficult
to determine accurately the volume of the interaction zone
as well as the product detection efficiency. For these
reasons, it is more pratical to measure relative cross
sections and normalize the results, if possible, to absolute
results from other experiments. In this study, quantities
(n_A' and n_B') proportional to the average beam densities are
measured. The photon flux, S_p, which is proportional to R,
is also measured. Since the product $n_A' \, n_B'$ is proportional
to the integral in (8), then $S_p = K' \sigma(v_r) v_r \, n_A' \, n_B'$ where K' is
a proportionality constant. If the relative intensity of A,
I_A, is measured instead of n_A', the cross section is given by

$$\sigma(v_r) = K \frac{S_p v_A}{I_A n_B' v_r} = K \, \sigma_{rel}(v_r) \qquad (9)$$

where v_A is the velocity of A, and $n_A' = \dfrac{I_A}{v_A}$ has been used.
The cross section is now expressed in terms of quantities
which are measured experimentally.

The cross section is related to the translational
thermal rate constant k(T) by

$$k(T) = \int_0^\infty \sigma(v_r) \; f(v_r) \; v_r dv_r = K \int_0^\infty \sigma_{rel}(v_r) \; f(v_r) v_r dv_r \qquad (10)$$

where $f(v_r)$ is the relative velocity distribution function. Thus, given $k(T)$ at a particular temperature and the experimental determination of $\sigma_{rel}(v_r)$, K may be determined and normalization accomplished. Note that, if the cross section is independent of v_r,

$$k(T) = \sigma \, \overline{v}_r \qquad (11)$$

where $\overline{v}_r$ is the average relative velocity. Conversion from $k(T)$ to σ is often done using (11) when information about the velocity dependence of the cross section is not available.

Equation (10) may be used to calculate $k(T)$ from cross section measurements. Since the cross section is usually measured as a function of the relative kinetic energy E_r of the reactants, it is convenient to express $k(T)$ in terms of E_r:

$$k(T) = (\tfrac{8\beta}{\pi\mu})^{1/2} \int_0^\infty E_r \, \sigma(E_r) dE_r \qquad (12)$$

where $\beta = \frac{1}{kT}$, k is the Boltzmann constant, μ is the reduced mass and the normalized Maxwell-Boltzmann relative energy distribution has been assumed.

D. The Penning Ionization Process

Theoretical attempts to explain the experimental measurements of Penning ionization cross sections have resulted in a fairly well-established picture of the dynamics involved. Early theoretical attempts had very few accurate measurements for testing their results. Ferguson[23] correlated momentum transfer cross sections (calculated from simple kinetic considerations) with experimental cross sections

for metastable helium reactions with the rare gases, nitrogen, and mercury. Bates et al.[24] proposed the formation of an initial collision complex $A^* + (XY)^* \rightarrow (AXY)^*$, and Penton and Muschlitz[25] suggested that competition between pre-ionization and dissociation of the collision complex could explain measured isotope effects and the presence of associative ionization products.

More recently, Penning electron spectroscopy results[26] indicate a direct mechanism, rather than complex formation. A physical description of the Penning process, called the electron exchange mechanism, has been given by Niehaus[27] and by Stedman and Setzer.[10] For $He(2^3S)$ colliding with N_2, the predominant interactions are between the electrons in the $5\sigma_g$, $4\sigma_u$, and π_u orbitals of N_2 and the half empty 1s orbital of $He(^3S)$. A nitrogen electron tunnels to the vacant 1s orbital of He and the helium 2s electron is ejected. This description is consistent with early observations that the reactivity of the metastable rare gas atoms in Penning ionization reactions increases with electron accepting ability.[28]

The presently accepted theoretical formulation of the Penning ionization process is due to Nakamura[29] and Miller[30] (the classical treatment discussed here follows Miller's closely).

Consider the following ionization processes:

$$A^* + XY \rightarrow A + XY^+ + e \qquad (13)$$
$$\rightarrow AXY^+ + e \qquad (14)$$
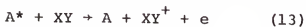
(13) and (14) are described in terms of the interaction potential curves of the reactant and product species. Figure 1 depicts these Born-Oppenheimer potential curves. $V[A^*-XY]$, the entrance channel interaction potential, is shown as purely repulsive although shallow attractive wells exist for many pairs (a well depth of 0.004 eV. has been measured[31] for He* - Ar). $V[A-XY^+(1,2,3)]$ are exit channel interaction potentials for three different electronic states of XY^+. These are depicted as attractive to allow for associative ionization (well depths for He - XY^+ are probably ≤ 0.1 eV.).[32] The shaded area denotes a continuum of states which dissociate to A + XY^+ + $e(\varepsilon)$ at R = ∞ where $e(\varepsilon)$ represents an electron with continuously variable energy ε. So, $V[A^*-XY]$ is embedded in the continua of all three exit channels.

For every value of R along the entrance channel there is a width $\Gamma(R)$ associated with $V(A^*-XY)$ in which transfer from the discrete electronic state to the continuum $V[A-XY^+(1,2,3) + \varepsilon]$ may occur. Thus $\Gamma(R)$ (which has the units of energy and represents a coupling between the channel and the continuum) is called the autoionization width. This coupling vanishes at infinite separation, i.e., $\Gamma(R) \rightarrow 0$ as $R \rightarrow \infty$. $\Gamma(R)$ may be obtained from electronic structure calculations with some difficulty. The kinetic energy, ε, of the electron for a transition to $V[A-XY^+(1)]$ is given by:
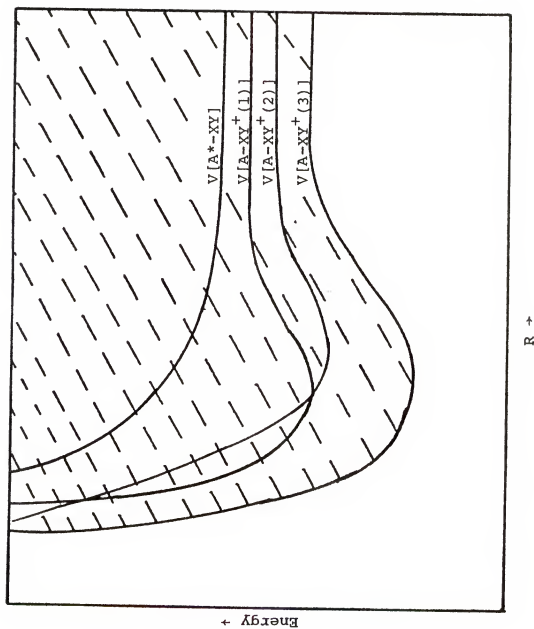
Figure 1. Penning Ionization Interaction Potential Curves

$$\varepsilon = V[A^*-XY]_R - V[A-XY^+(1)]_R - \Delta E_{vib} - \Delta E_{rot}$$

where ΔE_{vib} and ΔE_{rot} are the differences between the initial and final vibrational and rotational energies, respectively.

For atom-atom collisions, the spherical symmetry of the problem allows separate treatment of the radial motion for each value of the angular momentum ($\ell\hbar$). For metastable atom collisions with molecules, the lack of spherical symmetry may be ignored if R is large enough compared with the XY equilibrium internuclear distance. The appropriateness of this assumption for the He^*/N_2 system has been discussed by Hotop and Niehaus.[33]

Let $P_\ell^{in}(R)dR$ be the probability that transition to the continuum occurs in the interval $R \to R + dR$ on the incoming trajectory.

$$P_\ell^{in}(R)dR = [1-\int_R^\infty P_\ell^{in}(R)dR](\frac{\Gamma(R)}{\hbar})(\frac{dR}{v_\ell(R)}) \tag{15}$$

where the radial velocity $v_\ell(R)$ is given by

$$v_\ell(R) = (\frac{2}{\mu}[E-V(A^*-XY)-\frac{\ell^2\hbar^2}{2\mu R^2}])^{1/2} \tag{16}$$

By converting (15) to a differential equation and solving,

$$P_\ell^{in}(R) = \frac{\Gamma(R)}{\hbar v_\ell(R)} \exp[-\int_R^\infty \frac{\Gamma(R)}{\hbar v_\ell(R)}dR] \tag{17}$$

From (15) and (17),

$$\int_{R_0}^\infty P_\ell^{in}(R)dR = 1 - \exp[-\int_{R_0}^\infty \frac{\Gamma(R)}{\hbar v_\ell(R)}dR] \tag{18}$$

where R_0 is the classical turning point (that is, where $v_\ell(R) = 0$). Similarly,

$$\int_{R_0}^\infty P_\ell^{out}dR = \exp[-\int_{R_0}^\infty \frac{\Gamma(R)}{\hbar v_\ell(R)}dR](1-\exp[-\int_{R_0}^\infty \frac{\Gamma(R)}{\hbar v_\ell(R)}dR]) \tag{19}$$

(18) and (19) are the probabilities that transition to the continuum occurs somewhere along the incoming or outgoing trajectory, respectively. Thus the proability P_ℓ, of a transition during the entire collision is the sum of (18) and (19):

$$P_\ell = 1 - \exp[-2\int_{R_0}^{\infty} \frac{\Gamma(R)}{\hbar v_\ell(R)} dR] \qquad (20)$$

Finally, the cross section for total ionization is given by:

$$\sigma_T = \frac{\pi}{k_0^2} \sum_\ell (2\ell+1) P_\ell \qquad (21)$$

where $k_0^2 = \frac{2\mu}{\hbar^2}[E - V(A^*-XY)_\infty]$. Equations (16), (20), and (21) allow the calculation of σ_T if $V(A^*-XY)$ and $\Gamma(R)$ are known.

If the potential $V[A-XY^+]$ has sufficient well depth to support bound vibrational states, associative ionization may occur.

E.   The Excitation Transfer Process

By analogy with Penning ionization, the excitation transfer process leading to neutral products, reaction (1), has been visualized as an electron exchange mechanism.[10] In the Ar^*/N_2 case, an electron from the $4\sigma_u$ or $5\sigma_g$ orbital of N_2 occupies the vacancy in the argon 3p orbital, and the 4s electron of Ar enters the $2\pi_g$ orbital of N_2. In terms of the interaction potentials, a double curve crossing, similar to that proposed by Herschbach[34] for alkali atom reactions, was suggested:[10]   the first transition is from the $Ar^* - N_2$ curve to the $Ar^- - N_2^+$ coulombic curve; the second is from the coulombic curve to one of the open exit

channels, Ar + N_2*. The long collision duration required by such a mechanism, as well as various characteristics of the rotational spectrum of $N_2(C^3\Pi_u)$ observed in flowing afterglow studies, led to the proposal of a collision complex, ArN_2*, from which the observed excited states of $N_2(B^3\Pi_g$ and $C^3\Pi_u)$ are produced.

Piper et al.[35] pointed out that such a charge transfer curve crossing mechanism is not practical for Ar* collisions with a target gas that has an ionization potential greater than about 14 eV. (the ionization potential of N_2 is 15.6 eV.). In addition, a recent differential scattering study of Ar*/N_2 reports a backward-peaked Ar scattering distribution indicative of a direct, rather than complex, mechanism for excitation transfer.[36] Piper et al.[35] suggested a single curve-crossing mechanism. If the repulsive wall of the Ar* - N_2 potential rises at smaller internuclear separations than the repulsive wall of the Ar - N_2* potential, the input channel cannot cross exit channels which lie below it at $R = \infty$. However, internally excited states of N_2* may lie above the input channel and close enough in energy that the crossing may be reached in a thermal energy collision.

Regarding a process as starting on one potential energy curve and ending on another is a two-state approximation to the impact parameter method of calculating cross sections.[37] Most of the probability for transition is obtained from the region of the trajectory where the initial and final

potential curves come close to each other. The treatment, due to Landau and Zener,[38] yields and expression for the cross section, σ, as a function of relative velocity, v, for atom-atom collisions:

$$\sigma(v) = 4\pi R_0^2 [E_3(\frac{2\pi\beta^2}{\alpha\,v}) - E_3(\frac{4\pi\beta^2}{\alpha\,v})] \qquad (22)$$

where $E_3(z) = \int_1^\infty \frac{e^{-zy}}{y^3}\,dy$. Expressions for α and β are given in reference 37 - they are calculated from electronic Hamiltonian matrix elements. A discussion of the application of the Landau-Zener model to reaction (6) is given in Chapter VI.

F. Purpose and Scope of Present Study

The reactions, (6) and (7), chosen for this investigation have been thoroughly studied by many of the techniques mentioned in section IB. One reason for this is that the information desired here is of such a specific nature (cross sections for transfer from particular translational and electronic states to specific electronic states) that the results need to be interpreted by comparison with more general results (cross sections for total ionization or excitation for example). From a more practical point of view, the cross sections for reactions chosen for study on this apparatus must be large enough, to result in a measurable photon flux. The radiative lifetimes of $N_2(C)$ and $N_2^+(B)$ have been reported as 28 nsec. and 59 nsec. respectively,[39,40] so that all of the sensitized fluorescence occurs at the intersection region of the two beams. Total quenching cross

sections ($\overset{O}{A}{}^2$) of 5.8 ($^3P_2$) and 2.5 ($^3P_0$) have been reported for (6) at 300°K.[35] Total quenching cross sections of 12.5(2^1S) and 5.21(2^3S) have been reported for (7) at 300°K.[41] Typical photon flux measurements for these systems are given in Chapter IV. For various reasons, discussed in Chapter IV, fluorescence from N_2(B) and N_2^+(A) was not measurable.

The purpose of this investigation was to introduce a new technique for studying electronic energy transfer processes, measure the relative cross sections of reactions (6) and (7) as a function of the relative translational energy of the reactants, and interpret the results in such a way as to further elucidate the excitation transfer and Penning ionization mechanisms involved.

Chapter II is a description of the apparatus used. The vacuum system as a whole is discussed, and then the experiment is broken down into its various components -- metastable beam production and analysis, nozzle beam production and analysis, photon detection, and data handling. Chapter III presents data and calculations which describe the metastable and nozzle beams in terms of their intensities and their velocity distributions. Chapter IV describes general experimental procedures as well as details relating to the specific systems studied. In Chapter V the measured relative cross sections versus relative translational energy are presented and the reliability of the data is discussed.

Chapter VI is a discussion of the results of this study. Previous measurements relevant to the systems studied are examined and possible mechanisms which reconcile these measurements are discussed.

CHAPTER II

DESCRIPTION OF THE APPARATUS

A. Introduction

Figure 2 is a photograph of the main vacuum chamber
which is constructed from 2" thick aluminum. The apparatus
consists of three vacuum chambers, inlet manifolds for the
two crossed beams, and the electronic instruments required
for measuring the variables in equation (9).

A schematic drawing of the vacuum chambers and major
instrumentation is shown in figure 3. The metastable atom
beam is produced in a low voltage, D.C. discharge cell in
the discharge chamber (section IIC). The beam is formed by
effusion through a slit in the discharge cell and collimated
by two more slits prior to entering the velocity selector.
The velocity selector is a rotating, slotted-disc device
(section IID) which not only filters the atoms with respect
to speed, but also keeps direct light from the discharge cell
out of the main chamber. The beam exits the discharge chamber
through another narrow slit, passes between two sweep plates,
where charged particles are deflected out of the beam, and
intersects the target beam. A movable beam flag may terminate
the beam or allow it to hit the excited atom detector (either
a Faraday cup detector or an electron multiplier depending
on the experiment - see section IID).

Figure 2. Main Vacuum Chamber
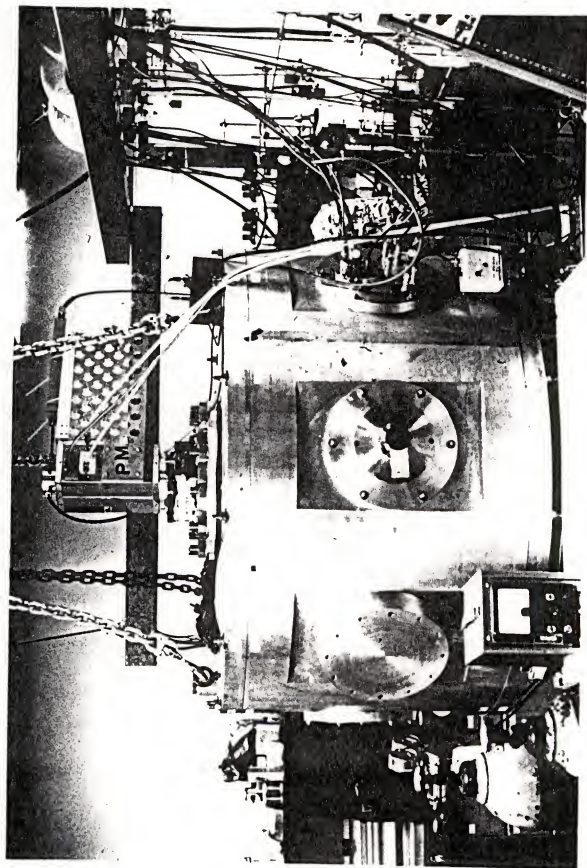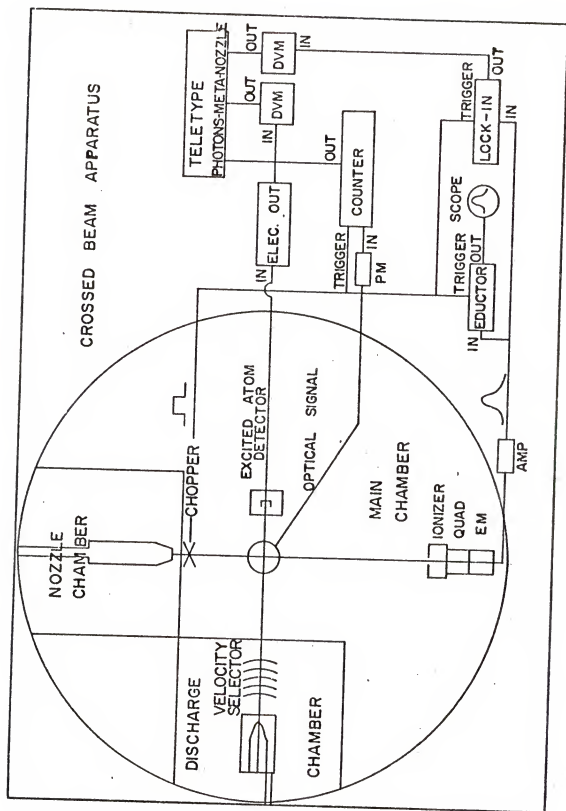
Figure 3. Crossed Beam Apparatus

The target beam is a supersonic nozzle beam formed by maintaining high target gas pressure behind a small orifice in the nozzle cap located at the end of an oven. The velocity of the target beam may be increased by the technique of seeding, or by increasing the temperature of the oven. The target beam exits the nozzle chamber through a specially designed skimmer mounted on the wall of the nozzle chamber, and enters the main chamber where it is collimated and, then, modulated by a mechanical chopper. After intersecting the metastable atom beam at right angles, the target molecules are detected by a quadrupole mass spectrometer, and velocity analyzed by time of flight (section IIF).

Light emission from the intersection region is measured by photon counting. Photons are collected (by a lens and a mirror located above and below both beams) and focused onto the cathode of a photomultiplier (section IIG). Pulses from the photomultiplier are amplified and counted by a dual channel counter. Signal averaging is accomplished by synchronizing the counter gates with the target beam modulation frequency.

The apparatus described above permits the measurement of all quantities necessary to calculate the relative cross section -- photon flux, metastable atom beam intensity and velocity, and target beam density and velocity. The main features are 1) a metastable atom beam velocity selected by a mechanical selector and velocity analyzed in a separate experiment by time-of-flight; 2) a nozzle beam whose velocity

is varied by seeding and velocity analyzed by time of flight; 3) detection of fluorescence in the intersection zone by photon counting and signal averaging. The various components of the apparatus are described in detail in the following sections.

B. Gas Inlet Manifolds and Vacuum Chambers

A schematic drawing of the manifold for delivering the gas used in the discharge is shown in figure 4. Helium or argon from Airco cylinders[42] passes through stopcock 1 into a liquid nitrogen or dry ice - acetone cooled trap. This serves to remove any condensable impurities which may effect the discharge, contaminate the filament, or attenuate the metastable atom beam. After passing through stopcock 3, the discharge gas pressure is reduced from a pressure of approximately three PSI to less than one torr by passing through a manually controlled leak valve. The leak valve is adjusted to give the desired backing pressure as read on a Wallace and Tiernan absolute pressure gauge[43a] or a Pirani gauge.[44] The Pirani gauge was originally calibrated for air and was not re-calibrated for argon or helium, so measurements using it are not accurate. It does, however, allow reproduction of discharge conditions from day to day. The Wallace and Tiernan gauge readings are not possible at the low pressures used in the argon discharge. Therefore the Pirani gauge was used for argon. The discharge gas then enters the dis-
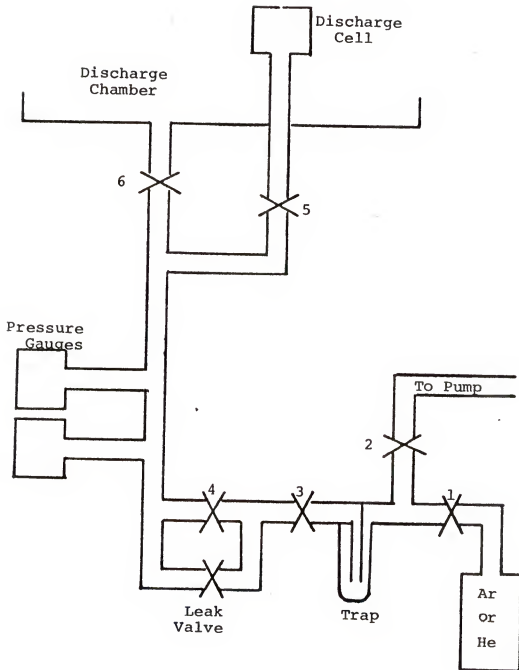
Figure 4. Discharge Gas Inlet Manifold

charge cell through valve 5. During normal operation valves 2, 4, and 6 are closed.

The discharge gas inlet manifold is evacuated by a Cenco roughing pump[45] until the pressure is low enough to open valve 6 and further evacuate the line through the discharge chamber pumps.

The target gas delivery manifold is shown in figure 5. If the target gas is pure nitrogen, valves 1, 2, and 10 only are opened and the nitrogen tank regulator valve is adjusted to give the desired backing pressure (typically 18 PSI) as read on a Wallace and Tiernan gauge.[43b] If the nitrogen beam is seeded with helium, valves 1, 3, 4, 10 and 5, 7, 8 are opened. All the valves, except 4 and 8, are shut-off valves. 4 and 8 are leak valves which are adjusted to give the desired flow rates as measured by Hastings mass flowmeters,[46] (FM). This system, with high pressures behind valves 4 and 8, allows independent control over both beam components over a wide range of pressures so that stable mixtures of any proportion are possible.

A 7 micron, mesh filter[47] (between valve 10 and the nozzle oven) removes any small particles which might clog the nozzle channel.

The target gas manifold is evacuated by a small roughing pump until the pressure (as read on a thermocouple gauge[48a]) is low enough to open valve 11, and further evacuate the line through the nozzle chamber pumps.
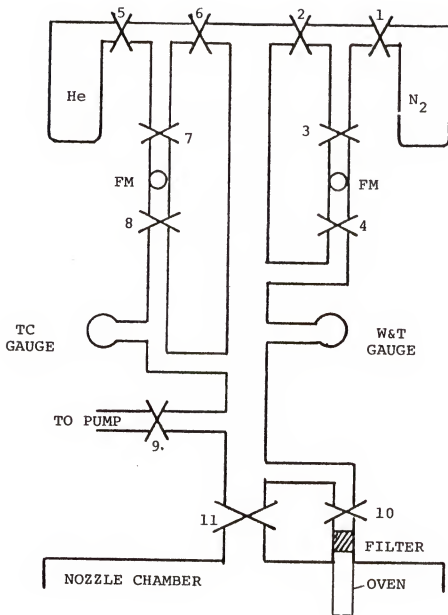
Figure 5. Target Gas Inlet Manifold

The discharge chamber is evacuated by an NRC 4" oil diffusion pump[49a] backed by a Welch roughing pump.[50a] An Ultek[51] foreline trap prevents contamination of the diffusion pump oil by the mechanical pump oil vapor. The discharge chamber pressure is monitored by an ionization gauge[52a] located on the back wall of the discharge chamber. The nozzle chamber is evacuated by a 6" oil diffusion pump[49b] (with a "Mexican hat" cap to prevent backstreaming of the diffusion pump oil into the nozzle chamber) and a Welch forepump.[50b] The nozzle chamber pressure is monitored by an ionization gauge[52a] located on the back wall of the nozzle chamber. The foreline pressures for both the nozzle and discharge pumps are monitored by NRC thermocouple gauges.[49c] The main chamber is evacuated by a 10" oil diffusion pump[48b] with a refrigerated baffle[53] and a roughing pump.[50c] The main chamber pressure is monitored by an ionization gauge[52a] located on the main chamber wall, almost directly behind the excited atom detector. The foreline pressure is monitored by a thermocouple gauge.[52b]

Typical static chamber pressures measured are recorded below:

Discharge chamber: 1×10^{-6} torr
Nozzle chamber: 1×10^{-7} torr
Main chamber: 2×10^{-6} torr

The diffusion pumps are protected in several ways. A relay which shuts off all three diffusion pumps may be triggered in two ways. If a leak causes the main chamber

foreline pressure to rise above 150 microns (this may be varied) the relay is triggered from the vacuum controller.[52b] If the main diffusion pump cooling water flow decreases below an adjustable level, then the relay is triggered from a water flow monitor.[54] Additionally, the 4" and 6" diffusion pumps have protective thermostats which prevent over-heating.

C. Metastable Beam Production

The low voltage, D.C. discharge cell is similar to the one used by Tang.[55] Figure 6 is a top view photograph of the discharge cell 1 and the velocity selector 2. The 2.6" long cylindrical cell has walls made from 50mm diameter quartz tubing. The back wall of the cell (away from the velocity selector) is a copper block with a hole for inserting and removing the filament assembly. The front wall (anode) of the cell is a circular copper plate with a 0.024" wide source slit. The anode is water cooled by a copper water line which runs about four-fifths of the way around the circumference. This prevents overheating of the source during operation at the high filament currents and voltages used in this study. It was necessary to keep reflected light from the discharge out of the main chamber by shielding the quartz cell with a cylindrical piece of aluminum mounted from the anode. Since the other end of this shield could not extend all the way to the back plate without shorting the anode to ground, a strip of quartz tape was wrapped around the gap. This shield makes the source somewhat hotter than Tang's source.

Figure 6. Discharge Chamber and Velocity Selector
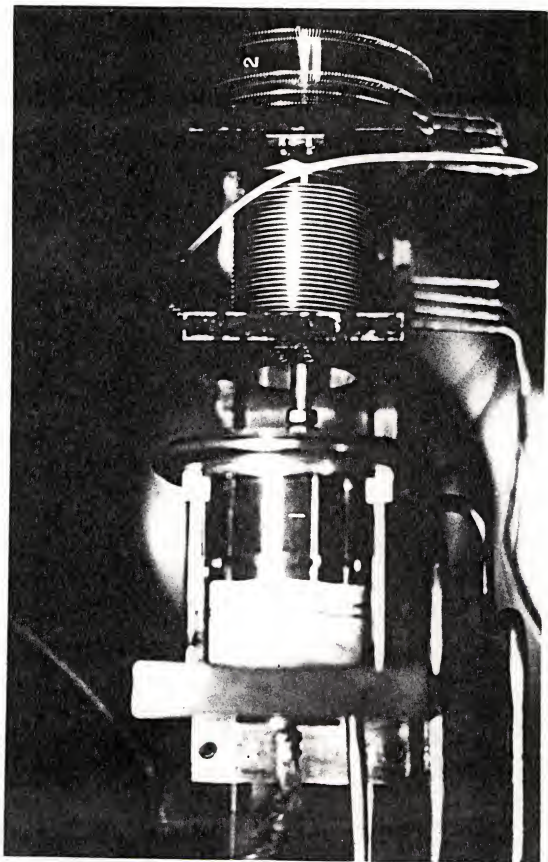
The filament assembly is shown in figure 7. The filament is a 2.7" long, 0.125" wide, tungsten ribbon, cataphoretically coated with thoria to reduce the work function.[56] It is spot welded between two nickel tabs which are spot welded to inconel studs. Two different stud lengths and several different filaments lengths were tried in order to find a combination that gave the maximum metastable atom intensity. Longer filaments than the one chosen tended to sag toward the bottom of the cell. The studs are press fit (also held with a set screw) over insulated feed throughs which carry the filament current from heavy, flexible copper braid, through the circular copper base which press fits into the grounded, copper block, to the filament. The flexible braid permits removal of the filament assembly without also removing the aluminum flange through which electrical connections are made to the vacuum system. The distance from the maximum extention of the filament to the anode is approximately 0.33".

Figure 8 is a schematic drawing of the discharge cir-cuitry. The filament is biased at +30 volts (from a Lambda power supply[57]) in order to reduce the destruction of the filament coating caused by positive ion bombardment. The filament current is supplied by a Trygon, current-regulated, D.C. power supply.[58] The anode voltage and emission current are controlled by a Sorenson D.C. power supply[59] which is operated in the current limiting mode. The emission current is set at the desired level, and the anode voltage is altered in order to maintain the desired emission current. The

ANODE

THORIA COATED
TUNGSTEN

Ni TABS

INCONEL
RODS

COPPER
PLATE

COPPER
BRAID
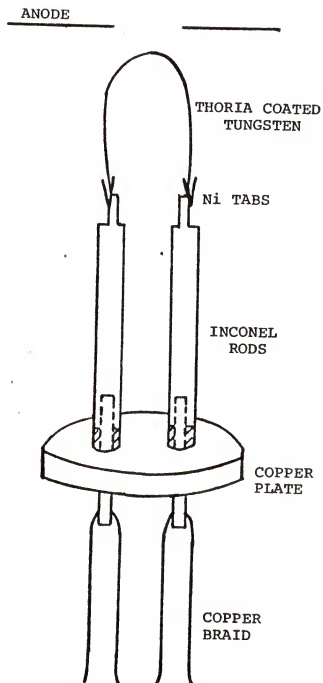
Figure 7.   Filament Assembly
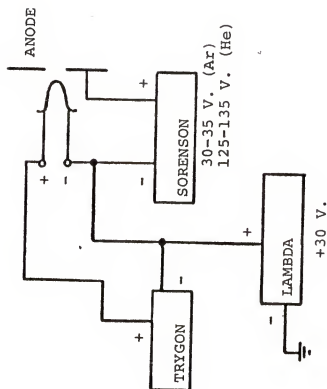
Figure 8. Discharge Circuitry

emission currents chosen represent a compromise between metastable intensity and filament lifetime. The discharge pressures, emission currents and anode voltages used in this study are given below:

Discharge Gas	Pressure (Torr)	Emission Current (amps)	Anode Potential (volts)
Argon	0.14	1.0	30
Helium	0.74	2.0	130

If argon is the discharge gas, the $^3P_{2,0}$ metastable states are formed as well as many other neutral and ionic excited states. All neutral states except the metastable states radiate long before leaving the discharge chamber. Any charged particles leaving the discharge chamber are removed from the beam by sweep plates in the main chamber. Therefore, the argon discharge source results in a beam of atoms containing only ground state and $^3P_{2,0}$ metastable argon atoms. Using a source similar to this one, Tang measured a $^3P_2/^3P_0$ ratio of approximately 7.[60]

If helium is used as the discharge gas, only the ground state and $2^{1,3}S$ metastable states remain in the beam. The singlet component is greatly reduced by superelastic collisions with electrons:[61]

$$He(2^1S) + e \rightarrow He(2^3S) + e$$

So, it is expected that the metastable helium beam used in this study consists mostly of triplet states, but the exact percentages of each component are not known.

D. Metastable Beam Velocity Selection and Analysis

After leaving the discharge cell through the slit in the anode plate, the metastable atom beam is collimated by passing through two slits mounted on aluminum plates which also support the motor for the velocity selector (see figure 6). These slits are 0.020" wide. The collimated beam then enters the velocity selector.

The velocity selector, shown in figure 9, is constructed according to the design of Grice.[62] Its short rotor length (slightly over one inch) is convenient, and contributes to its relatively high transmission. The five selector discs, made of Alcoa 2024-T3 aluminum alloy, are four inches in diameter and each has 248 slots. By inserting two parallel rods through alignment holes (180° apart on each disc), proper positioning of the discs relative to each other was insured. The calculation of the proper angular and spatial relationships of the discs is discussed by Kinsey.[63] The discs and aluminum spacers slip over an aluminum arbor which is screwed directly to the motor shaft. In this respect, the Grice design differs from earlier velocity selector designs. The light weight of the rotor and the mounting design minimizes the problem of motor vibration. The motor is press fit into an aluminum cylinder cut with grooves. Wrapped through these grooves are taut phosphor bronze windings, the ends of which are attached to the same aluminum uprights which hold the collimating slits. The end of the motor opposite the selector discs is counter-balanced by a spring

Figure 9. Velocity Selector
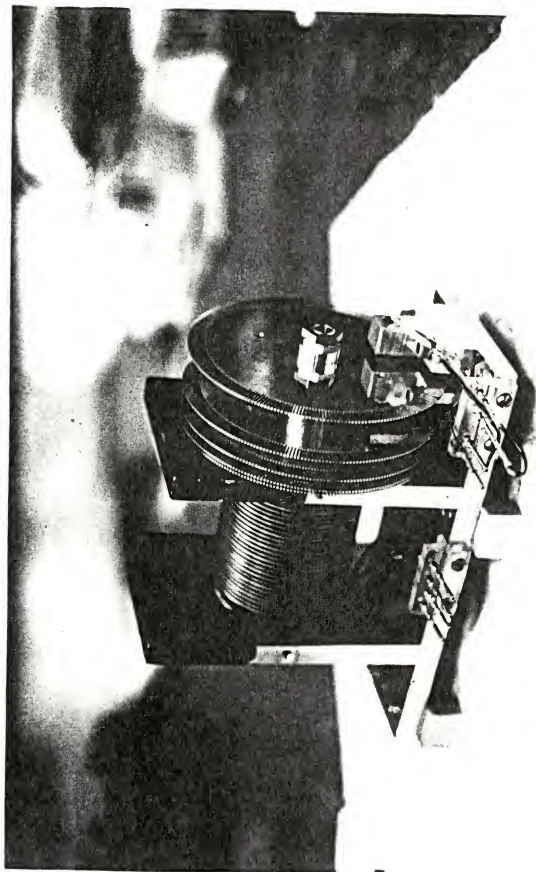
attached to a brass shaft extending out the rear of the motor. The other end of the spring is connected to the base plate supporting the aluminum uprights. Thus, the motor is free to find its own axis of rotation.

The motor is a TRW, 400hz., synchronous, hysteresis motor[64a] which is driven by a California Instruments oscillator[65a] whose output is amplified by an Invertron wide band amplifier.[65b] The selector frequency is varied over the range of 50 herz to 450 herz by changing the oscillator frequency and coupling capacitor to the appropriate values. A schematic drawing of the motor circuitry is shown in figure 10.

Several motor bearings were tried.[66] All of them tended to get very hot at frequencies greater than 350 herz. Even Barden bearings coated with a teflon coating by Ball Brothers, which worked well for Tang,[67] were ruined by the high temperature. The bearings, located inside the motor casing, were apparently heated not only by frictional contact with the shaft, but also by the motor itself. After some minor modifications to aid heat dissipation, it was decided to monitor the temperature carefully (via a chromel-alumel thermocouple inserted into the brass shaft very close to the rear motor bearing), and lubricate the bearings periodically with a lubricant obtained from Ball Brothers.[68]

The base plate, onto which the aluminum motor supports are fastened, is slotted in such a way as to allow the rear upright to be moved closer to or farther away from the other

frequency (hz.)	capacitance (µF.)
100	0.87
200	0.43
300	0.32
400	0.20
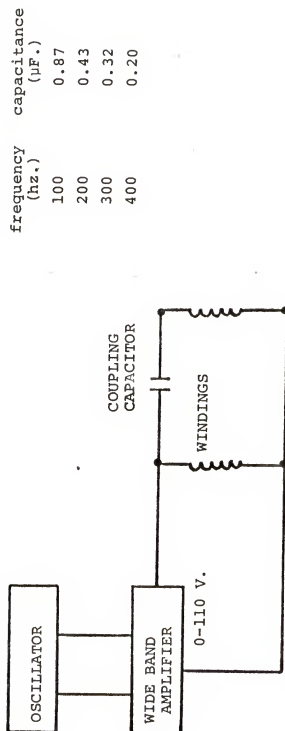
Figure 10. Velocity Selector Motor Circuit

upright, and tilted as desired. In this way, the spring
mount (and, thus, the selector discs) can be adjusted so
that the disc faces are always perpendicular to the beam
path. The underneath side of the base plate was cut length-
wise with two parallel, cylindrical grooves, which fit exactly
over two parallel, aluminum rods mounted from the base of
the chamber. Once set on these rods, the velocity selector
could be slid easily forward or backward while maintaining
the slit alignment.

The frequency of rotation of the selector discs is mea-
sured directly. A light emitting diode[69] is mounted between
the last two discs so that it lines up with one of the same
holes used for alignment purposes. A photodiode[70] is mounted
behind the last disc along the same line. The photodiode
pulses enter a shaping circuit, described in appendix II and
are counted by a pulse counter made in this laboratory.
Since there are two alignment holes, the measured frequency
must be divided by two. Figure 11 is a schematic drawing of
the frequency counting circuitry.

The relation of the various velocity selector parameters
to the transmitted beam velocity has been discussed by
Hostettler and Bernstein[71] whose notation is used in this
description. The parameters for two sets of discs are
defined and listed in Table I.

As used in the present study, the term nominal velocity
denotes the velocity corresponding to maximum transmitted
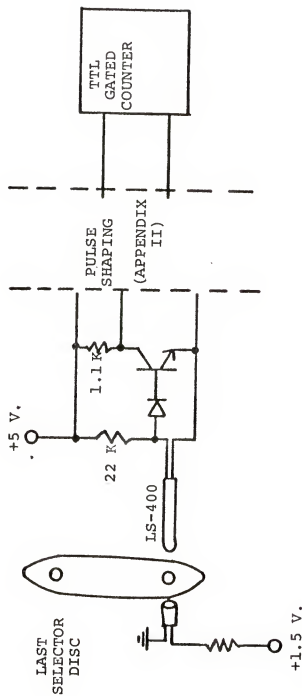
Figure 11. Velocity Selector Frequency Measurement

TABLE I

Parameters For Velocity Selector Discs

Parameter	Definition	Set I	Set II
ℓ_1	slot width	0.022"	0.022"
ℓ_2	average tooth width	0.0255"	0.0255"
η	$\dfrac{\ell_1}{\ell_1 + \ell_2}$	0.463"	0.463"
r	radius of disc	1.86"	1.86"
ϕ	helix angle	2°	3°
γ	$\dfrac{\ell_1}{r\phi}$	0.339	0.226
d	disc thickness	0.031"	0.031"
L	length of rotor	1.229"	1.186"
β	d/L	0.0252	0.0261
R	resolution = $\dfrac{\gamma-\beta}{1-\gamma}2$	0.355	0.261
G	transmission = $\eta r (1-\dfrac{\beta}{\gamma})^2$	0.135	0.081
λ	$\dfrac{2\pi L}{\phi}$	5.622m	3.610m
f	rotational frequency		
v_0	λf		
v_{max}	$(\dfrac{1-\beta}{1-\gamma})v_0$	$1.475v_0$	$1.258v_0$
v_{min}	$(\dfrac{1+\beta}{1+\gamma})v_0$	$0.765v_0$	$0.837v_0$

beam density. The quantity v_0 is the velocity which the velocity selector transmits most efficiently.

The intensity distribution of the transmitted beam, $T(v_0)$, is related to the intensity distribution of the incident beam, $I(v)$, and the velocity selector slit function $B(v)$, by the equation

$$T(v_0) = \int_{v_{min}}^{v_{max}} I(v) \ B(v) dv \qquad (23)$$

where $B(v) = B_1(v)$ or $B_2(v)$ and $B_1(v) \sim 1 - [(1+\beta)\frac{v_0}{v} - 1]\gamma^{-1}$ applies for $v_{min} < v < v_0$ and $B_2(v) \sim 1 + [(1-\beta)\frac{v_0}{v} - 1]\gamma^{-1}$ applies for $v_0 < v < v_{max}$. If, as Tang discovered in his analysis,[72] discharge conditions are such that the beam is an effusive one,

$$I(v) \sim v^3 e^{-mv^2/2kT} \qquad (24)$$

The temperature of the source may be estimated by finding the value of the temperature in (24) which makes $T(v_0)$ in (23) best fit the experimental measurement of transmitted intensity versus velocity.

It should be noted that the velocity corresponding to the maximum intensity at a particular selector frequency is not necessarily v_0; v_0 is the velocity for which the slit function $B(v)$ is a maximum. If $I(v)$ is changing rapidly over the range v_{min} to v_{max}, the velocity corresponding to maximum intensity will differ significantly from v_0. This effect is discussed with the presentation of metastable beam characterization measurements in Chapter III.

$T(v_0)$ is measured experimentally with the excited atom detector (Faraday cup) located as shown in figure 3. The metastable atom beam passes through a 0.040" wide slit and impinges on a gold surface, ejecting secondary electrons. The secondary electrons are drawn away from the gold surface to the walls of the surrounding chamber by a potential of 45 volts. A schematic drawing of the Faraday cup is shown in figure 12. The resulting current is measured with a Keithly electrometer[73] employing a 10^{11} ohm input resistor. This current is proportional to the excited atom flux which is monitored continuously during the experiment and included in the cross section calculation as discussed in section IC.

In order to evaluate the performance of the velocity selector, a time-of-flight analysis of the metastable atom beam was carried out in a separate experiment. A chopper was mounted immediately behind the discharge chamber exit slit in the main chamber. A schematic drawing of the chopper is shown in figure 13. It is similar to the nozzle beam chopper; and a detailed description of the circuitry, instrumentation, and procedure used for measuring the velocity distribution is given in the nozzle beam analysis (section IIF). The two analyses are identical except that the metastable atom detector is a Bendix magnetic electron multiplier[74] while the nozzle beam detector is an electron beam ionizer. Figure 14 is a schematic drawing of the magnetic electron multiplier, mount, and associated circuitry. The Faraday cup, used to measure the relative metastable atom intensity in
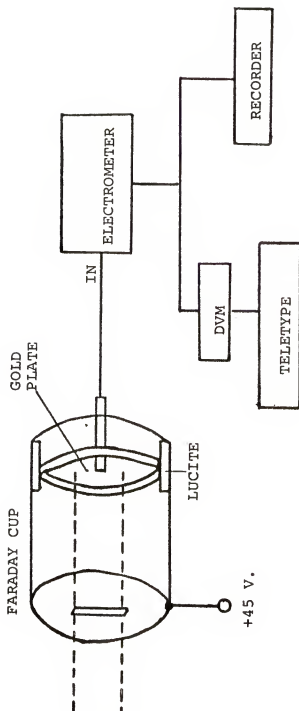
Figure 12. Faraday Cup Excited Atom Detector
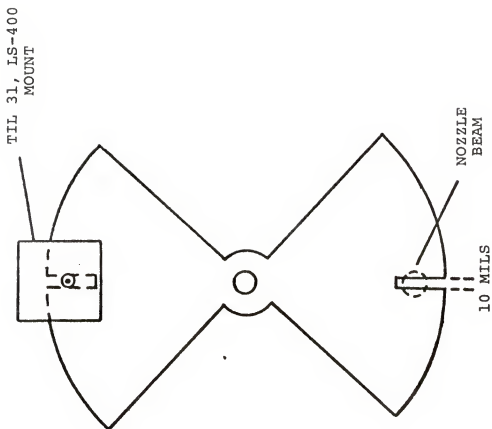
Figure 13. Metastable and Target Beam Chopper
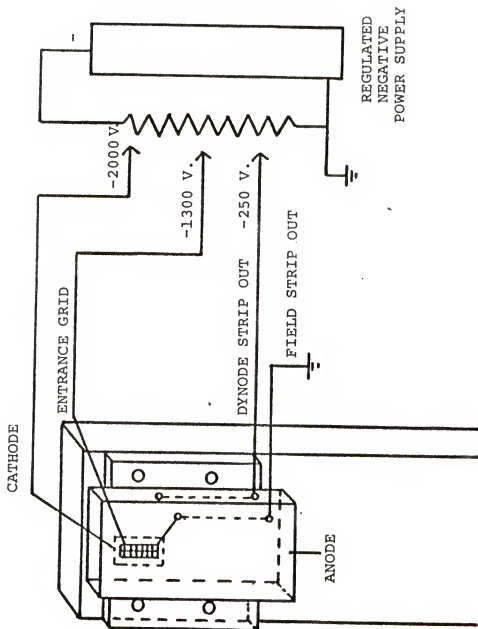
Figure 14. Magnetic Electron Multiplier

the fluorescence experiments, responds much too slowly to
intensity changes to be used for the time-of-flight analysis.
On the other hand, the electron multiplier was not as desir-
able for continuous intensity monitoring due to significant
zero drift.

The intensity and velocity characteristics of the
metastable atom beam are presented and discussed in section
IIIB.

E. Nozzle Beam Production

The target beam in this study is a supersonic nozzle
beam. The primary advantages of such nozzle beams over
effusive beams (increased intensity and narrow velocity
distribution) as well as other useful features have been
discussed by several authors.[75]

A schematic drawing of the components[76] which form the
nozzle beam is shown in figure 15. The nozzle oven is an
inconel cylinder, 4" long, 0.375" internal diameter, 1"
outer diameter. The cap is a truncated cone, made of inconel,
with a 0.002" diameter hole drilled through a 0.010" channel.
The skimmer is a hollow, brass cone with a 0.040" diameter
opening in the tip. The skimmer is screw-mounted to the
exit wall of the nozzle chamber and serves the purpose of
removing unused gas and defining the beam path in the region
of high gas pressure. The nozzle cap is screw-mounted to
the end of the oven. The oven itself is mounted on an
aluminum rod which may be extended toward or withdrawn from
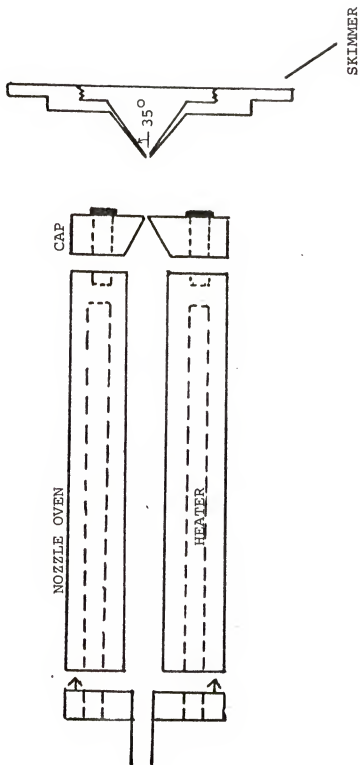
Figure 15. Nozzle Oven, Cap, and Skimmer

the skimmer by a screw mechanism operated through the vacuum chamber wall. The nozzle cap to skimmer distance is read on a micrometer dial actuated by the external end of the aluminum rod. The oven is connected to the target gas inlet by a flexible copper tube to allow the required oven movement. This nozzle source design allows interchangeability of nozzle caps and skimmers as well as optimization of nozzle beam intensity and velocity distribution with respect to nozzle-skimmer distance.

The channeling of internal energy and random translational energy into translational energy E_z directed along the beam axis produces the nozzle beam characteristics of increased energy and intensity as compared with effusive beams. By assuming that the expansion from the nozzle source is isentropic and that radial flow conditions exist, the ratio of the beam temperature T to the oven temperature T_0 may be estimated. In the limit of complete expansion, conservation of enthalpy[77] permits calculation of the beam energy from

$$E_z = C_p T_0 \quad (25)$$

where $C_p \simeq \dfrac{7k}{2}$ for nitrogen.

Theoretical nozzle beam intensities and velocity distributions have been discussed by Anderson and Fenn[78] who derived the following expression for the relative density as a function of relative flight time:

$$\frac{S}{S_{max}} = \frac{1}{\tau 4} \exp\{-\frac{1}{2}M_S^2[(\frac{b}{\tau}-1)^2 - (b-1)^2]\} \quad (26)$$

$$b = \frac{1}{2}[1 + (1+16/\gamma M_S^2)^{1/2}]$$

where S/S_{max} is the ratio of the beam density at a particular flight time to the maximum beam density, τ is the ratio of the time-of-flight to the time-of-flight for which S is a maximum, M_S is the Mach number at the skimmer entrance, and γ is the heat capacity ratio C_p/C_v. The Mach number is defined as the ratio of the bulk stream velocity u to the speed of sound in the gas: $M_S = \dfrac{u}{(\gamma kT/m)^{1/2}}$. Using equation (26), the Mach number which best characterizes the nozzle beam may be estimated by comparison with the experimentally determined velocity distribution. Further discussion of nozzle beam intensity and velocity distributions is included with the nozzle beam characterization experiments in Chapter IIIC.

The translational energy of the nozzle beam may be increased by heating the source or by mixing the primary beam gas with a lighter one. At the high densities of the nozzle source, both components will have the same velocity; but because of the different masses, the beam energies will be different.[77] In such a beam, the energy of molecule i is given by $E_i = \dfrac{M_i}{\overline{M}} \overline{C}_p T_0$ where M_i is the molecular weight of component i, $\overline{M}$ is the average molecular weight, and $\overline{C}_p$ is the average molar heat capacity. Seeding can have a significant effect on the beam geometry at the interaction zone. This problem is discussed in Chapter III.

F. Nozzle Beam Analysis

The target gas exits the nozzle chamber through the skimmer. The beam is further defined by passing through a 0.079" diameter collimator. The beam is modulated by a

chopper mounted on the main chamber side of the wall separat-
ing the two chambers. The same mount holds the collimator.
The chopper motor is a TRW, 60 hz. synchronous, hysteresis
motor[64b] which is driven by a Krohn-Hite oscillator[79a] whose
output is amplified by a Krohn-Hite wide band amplifier.[79b]

Modulation of the target beam accomplishes three pur-
poses. It permits phase sensitive measurement of the nozzle
beam intensity, determination of the beam's velocity profile,
and signal averaging of the photon flux. The chopper design
(figure 13) allows all of these functions to be performed
simultaneously. Two long beam pulses and two short pulses
are produced with each revolution of the chopping wheel.
Accompanying each beam pulse is an electrical signal from
the photocell[69,70] located 180° from the beam position. The
short pulses are formed when the narrow (0.010") slot
traverses the beam. This short beam pulse travels from the
chopper across the main chamber (21.20") to the nozzle beam
detector where it is velocity analyzed as discussed below.
The long beam pulses (5.0 msec. wide) provide the majority
of the beam molecules contributing to the sensitized fluores-
cence and relative target beam density measurements.

The nozzle beam detector is an EAI quadrupole mass
spectrometer,[80a] shown schematically in figure 16. The beam
is collimated prior to entering the ionization chamber by
a 0.070" wide slit. Ionization is accomplished by electron
impact (45 eV. electrons in these experiments). The ions
formed were drawn into the quadrupole and mass analyzed. The
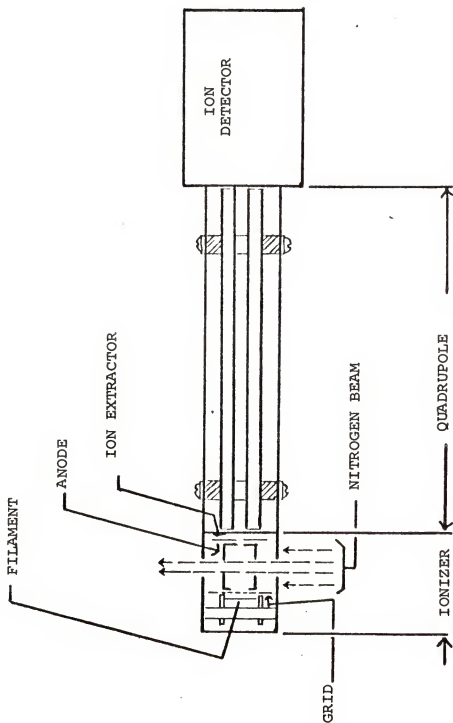
Figure 16. Target Beam Detector

quadrupole is set at mass 28(N_2^+) in order to detect the
primary target gas in the presence of the seeding gas. The
current pulse from the electron multiplier[80b] is converted to
a voltage pulse and further amplified by a fast response
two-stage amplifier circuit shown in Appendix I.

The pulses from the photocell provide the reference for
phase sensitive detection of the target beam intensity and
the trigger for the velocity profile measurement. The alter-
nating long and short pulses are first shaped into square waves
and then separated into separate trains of long and short
pulses by the circuit described in Appendix III. Square pulses
longer than 1200 μsec. qualify as long pulses and become
available at one output while those square waves which are
shorter than 800 μsec. are provided at the other output.

The relationships between photocell pulses (henceforth
called optical pulses) and beam pulses as detected by the
ionizer-mass spectrometer are depicted in figure 17.

The output of the first stage of the beam pulse amplifier
(Appendix I) is fed to the signal input of a PAR, lock-in
amplifier[81a] whose reference is provided by the long optical
pulses. Thus, only those signals with a 100 hz. component
are detected; and, additionally, signals with a 100 hz. com-
ponent but out of phase with the reference are not amplified.
Since beam pulses are slightly out of phase with optical
pulses by an amount corresponding to the flight time, a phase
adjustment, provided as a front panel control, is made for
each target beam velocity.

Figure 17. Pulse Timing Relationships

A. Output from pulse shaping circuit

B. Short pulses for triggering waveform eductor

C. Long pulses for triggering lock-in amplifier

D. Long pulses, delayed 200 μsec. for triggering SSR

E. Output from I → V converter/amplifier

$$\Delta t = \text{time-of-flight}$$
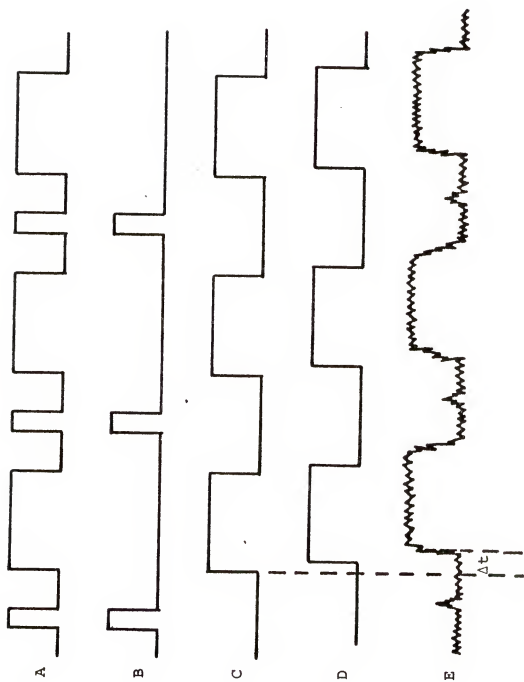
Since the feedback resistor of the current-to-voltage converter is $10^5 \Omega$, the electron multiplier anode current due to the modulated target beam is given by the lock-in voltage reading divided by $10^5 \Omega$. A typical lock-in voltage measurement for a pure nitrogen nozzle beam was 2 mV. so that the 100 hz. component of the anode current is approximately 2×10^{-8} amp.

The output of the second stage of the beam pulse amplifier is fed into a PAR, waveform eductor[81b] triggered by the short optical pulses. The waveform eductor has 50 channels, a variable sweep width (50 μsec. to 5.5 sec.), and a variable delay (10 μsec. to 11 sec.) between arrival of the triggering pulse and the beginning of the sweep. The delay is determined by measuring the time between the arrival of the triggering pulse and the production of a gating pulse (which starts the sweep) on a dual beam oscilloscope.[82a] The variable delay allows shorter sweeps and, thus, better resolution in terms of the number of μsec. per channel. Once the delay is accurately known, the nominal flight time (the flight time corresponding to maximum density) is read directly from an oscilloscope where the beam profile from the eductor output is displayed.

Figure 18 is a photograph showing the spatial relationships of the beam chambers and detectors. Magnetic beam flag 1 designed for the metastable atom beam was not used in any of these experiments; repeated mechanical failure

Figure 18.   Inside of Main Chamber
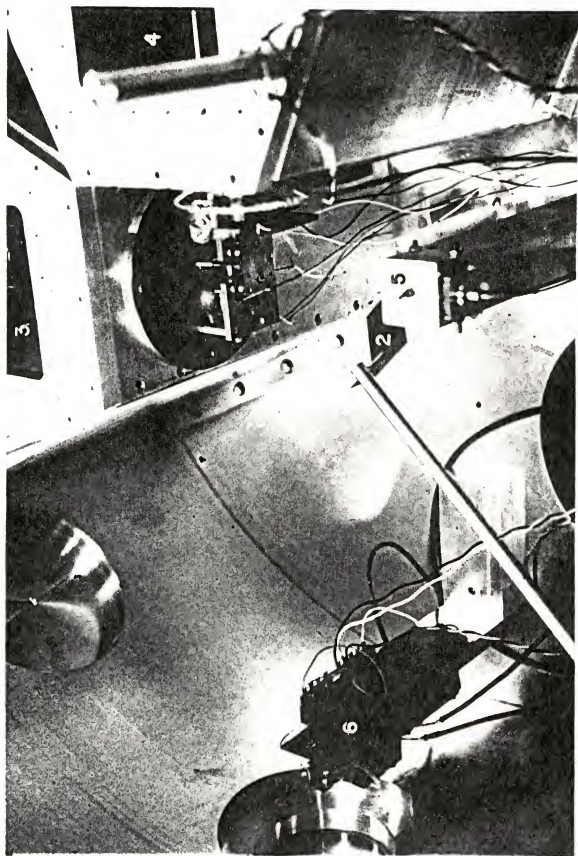
finally resulted in its replacement by the manually rotated beam flag 2 for purposes of zeroing the electrometer. The other components are labeled as follows: discharge chamber-3, nozzle chamber-4, Faraday cup-5, ionizer-mass spectrometer-6, chopper-7.

Measurements of the nozzle beam velocity profile are presented in section IIIC along with calculations of relative beam intensities and nominal velocities.

G. Photon Collection and Detection

Fluorescence from the intersection region is collected and focused on the photomultiplier cathode by the optics shown in figure 19. An aspheric condensing lens[83a] made of ordinary crown glass is located at a distance above the intersection region roughly equal to the focal length (38.1 mm). A concave mirror[83b] is located at its radius of curvature (34 mm) away from the intersection zone. Therefore, it reflects light back through the interaction zone to be collected by the lens.

The conically shaped, aluminum light baffle helps eliminate stray reflected light. The lens, mirror, and light baffle are mounted inside an aluminum tube (3" in diameter) which is fastened to the lid of the main chamber (see figure 19). The approximately parallel light rays exit the vacuum system through a Pyrex window mounted in a flange to the lid of the chamber. The optical tube helps keep reflected stray light from being detected as background noise. The openings
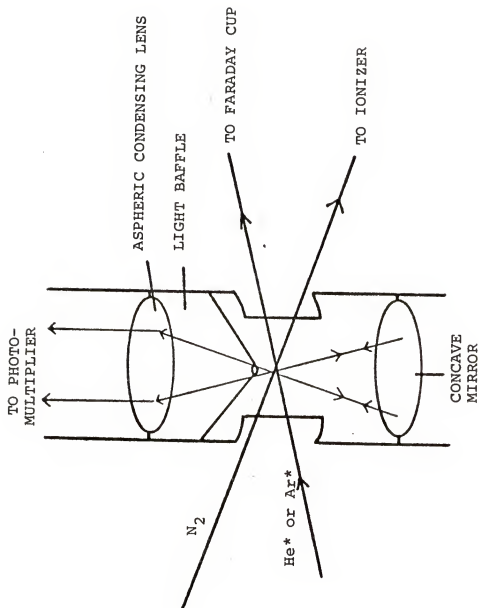
Figure 19. Photon Collection

in the tube at the beam entrances are large enough that
pumping the residual gas out of the tube is not a problem.

Light leaving the vacuum chamber strikes the S-20
cathode (with extended red response) of an EMI photomulti-
plier.[84] It is cooled with a Products for Research thermo-
electric refrigerator[85] to -25^0C under which conditions the
dark noise is approximately 10 counts/sec, at a bias potential
of 1250 volts supplied from a Northeast power supply.[86] The
location of the photomultiplier (PM) on the lid of the main
chamber may be seen in figure 2. Directly above the Pyrex
window is an aluminum tray for the purpose of inserting
appropriate filters between the window and the cathode.
Above this tray, a manual shutter seals off the multiplier
from radiation when photon measurements are not being made
and when the dark noise contribution to background is deter-
mined.

The wavelength response of the detection system is
effected by the transmission efficiency of the optics and
the quantum efficiency of the extended S-20 cathode. Figure
20 shows these efficiencies as a function of the emitted
photon wavelength. The significance of these response char-
acteristics is discussed in Chapter IV.

Pulses from the photomultiplier are amplified by an SSR,
linear amplifier,[87a] and counted by an SSR digital synchronous
computer.[87b] This dual channel photon counter while operating
in the "chop" mode stores counts in one of two channels
determined by pulses received at its trigger input. The gating
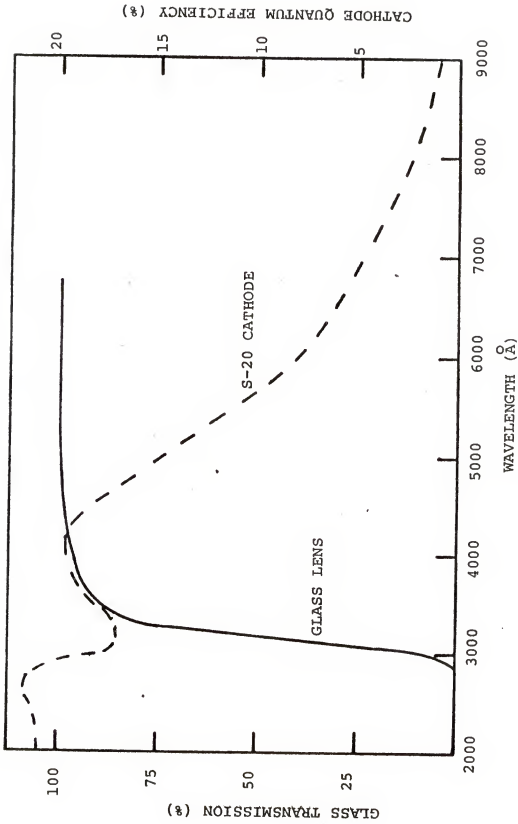
Figure 20. Wavelength Response of Lens and Phototube

is accomplished by the long optical pulses from the nozzle beam chopper. The same long pulses which trigger the lock-in amplifier are fed into a Hewlett-Packard pulse generator[82b] operated in the pulse delay mode. In this way, the long optical pulse is reproduced exactly except that it is delayed by 200 µsec. (which is plenty of time for the target beam to travel the approximately 2.2" from the chopper to the inter-section zone). The pulses from the pulse generator trigger the dual channel counter. When a positive pulse is received at the trigger input, scaler A accumulates counts corresponding to fluorescent emission plus background. When the pulse goes to zero, scaler B accumulates counts corresponding to back-ground only. An important feature of the SSR counter is that its internal clock insures that the counting time (ad-justed by a rear panel control) for each channel is exactly the same. For 4.0 msec. out of the 5.0 msec. (for 100 hz. modulation) corresponding to a beam pulse, counts accumulate in scaler A. The next 1.0 msec. is dead time. When the pulse goes to zero at 5.0 msec., counts accumulate in scaler B for 4.0 msec. After a 1.0 msec. delay the process is repeated for the number of cycles pre-set on a front panel control. The difference in the number of counts in scalers A and B corresponds to counts due to fluorescent emission only - all other contributions should average to zero. The long dead time of 1.0 msec. is not characteristic of the counter itself, but it was chosen because it makes timing errors (such as

those caused by slight variations in the oscillator fre-
quency) insignificant. The accumulated counts in scalers
A and B, as well as their sum and difference, are available
as output.

H.   Data Handling

The outputs of the electrometer and lock-in amplifier
are recorded by a Leeds and Northrup,[88] dual channel chart
recorder. They are also displayed digitally on two Digitec,
digital voltmeters[89a] (DVM in figure 3).

The two digital voltmeters and the photon counter are
interfaced to a teletype[90] with an interfacing system.[89b]
When the desired number of cycles (pre-set on the photon
counter) is reached, the contents of scalers A and B, their
sum, and their difference are printed on one teletype line.
On the next line are printed the panel meter readings which
are frozen at the instant that printing of the second line
begins. The counting process begins again automatically
unless the interface is in the manual mode, in which case
data collecting ceases until manually re-started. The
counting process is continued until suitable statistics
are obtained as described in Chapter V.

I.   Modifications of the Present Apparatus

Several modifications (some already in progress and
others in the planning stage) promise to increase the inform-
ing power and efficiency of the existing apparatus.

The major modification (which is now completed) is the installation of a Spex Minimate monochromator[91] with a dispersion of 40 $\overset{\circ}{A}$/mm. Whereas the present measurements are capable of separating photon emission contributions from different electronic states only, the addition of the mono-chromator to replace the optical filters will allow separation of contributions from different vibrational levels. This capability combined with the flowing afterglow technique has been very informative and promises to be extremely powerful when employed in beam studies of the translational energy dependence of electronic energy transfer. With the installa-tion of the monochromator, low fluorescent intensity becomes the major problem. This problem may be partially alleviated by removing the fifth velocity selector disc (at the cost of reduced metastable beam resolution), thereby substantially increasing the metastable atom beam intensity. The nozzle beam intensity may be increased by an improved nozzle with a smaller orifice. If necessary in the future, nozzle beam production may be improved with faster pumps to allow greater oven pressures. Another possibility for increasing the fluorescent intensity is conversion of the discharge source to a nozzle beam source in which metastable atoms are pro-duced by electron impact.

CHAPTER III

BEAM CHARACTERIZATION EXPERIMENTS

A. Beam Geometries

Relevant distances and slit widths for the metastable atom beam are presented in Table II. All slits are 0.25" in height. From these dimensions it is found that, in the center of the intersection zone, the metastable atom beam is 0.35" high and 0.040" wide.

Relevant distances and slit widths for the nozzle beam are presented in Table III. At the center of the interaction zone, the nozzle beam is 0.132" in diameter. Therefore, the interaction zone is approximately a cylinder with a base diameter of 0.132" and a height of 0.040"; and the intersection volume is about 4.7×10^{-4} in.^{3} or 7.7×10^{-3} cm.^{3}

B. Characterization of Metastable Atom Beams

Metastable atom beam intensities may be estimated from the secondary electron current measured by an electrometer, the secondary electron ejection coefficients and the beam geometry. The secondary electron ejection coefficients[92] are 0.66 for $Ar(^3P_{2,0})$ and 0.63 for $He(2^3S)$. For both helium and argon, the maximum electrometer signal, under the discharge conditions listed in section IIC and with the $2°$ discs was approximately 220 mV. corresponding to a current of 2.2×10^{-12} amp. For argon, the number of atoms detected

TABLE II

Metastable Atom Beam Dimensions

A. Slit Widths (in.)

discharge cell slit	0.024
selector mount slit	0.020
discharge chamber exit slit	0.036
Faraday Cup entrance slit	0.040
Bendix MEM entrance slit	0.010

B. Distances (in.)

discharge cell slit to velocity selector slit 1	1.73
velocity selector slit 1 to velocity selector slit 2	3.00
velocity selector slit 2 to discharge chamber exit slit	3.55
dishcarge chamber exit slit to chopper	1.40
chopper to intersection zone	2.00
intersection zone to Faraday cup entrance slit	5.05
intersection zone to Bendix MEM entrance slit	15.90

TABLE III

Nozzle Beam Dimensions

A. Orifice diameters and slit widths (in.)

    nozzle orifice   0.002

    skimmer orifice   0.040

    collimator orifice   0.079

    ionizer entrance slit width   0.070

B. Distances (in.)

    nozzle to skimmer   0.45

    skimmer orifice to collimator   2.80

    collimator to chopper   0.40

    chopper to intersection zone   1.85

    intersection zone to ionizer slit   18.95

per sec. is given by $(2.2 \times 10^{-12} \text{ amp})(1/1.6 \times 10^{-19} \text{ coul.}$ per electron) (1.52 atoms/electron) or 2.1×10^7 atoms/sec. The solid angle subtended by the Faraday cup slit is found from the ratio of the slit area to the square of the source slit - Faraday cup distance to be 3.6×10^{-5} steradians. Thus, the maximum metastable argon beam intensity observed was 6×10^{11} atoms/steradian sec. The result for helium was nearly the same.

Using equation (23) of section IID, the transmitted intensity distribution function $T(v_0)$ was calculated for argon using parameters for the 2^0 velocity selector discs (set I). By comparison with the measured intensity distribution, it was found that a temperature of 650^0K gives the best fit for the assumed Maxwell-Boltzmann distribution. A comparison of the calculated and experimental distributions is shown in figure 21. The integrals of equation (23) were evaluated (using Simpson's Rule) on a programmable calculator.[93] The experimental results were obtained by measuring the relative intensities with the Faraday cup detector at various velocity selector frequencies f, and calculating v_0 from $v_0 = \lambda f$.

The experimentally determined $T(v_0)$ distribution for helium is shown in figure 22. Since the peak of the distribution is not reached, no attempt was made to fit a theoretical curve to the experimental one.

Figure 21 indicated that the velocity selector is working properly. However, in order to be certain that there were

Figure 21. Experimental and Calculated Argon Intensity Distributions

— Theoretical $T(v_0)$ distribution assuming $I(v) \sim v^3 \exp[-mv^2/2kT]$

■ Experimentally measured intensity distribution
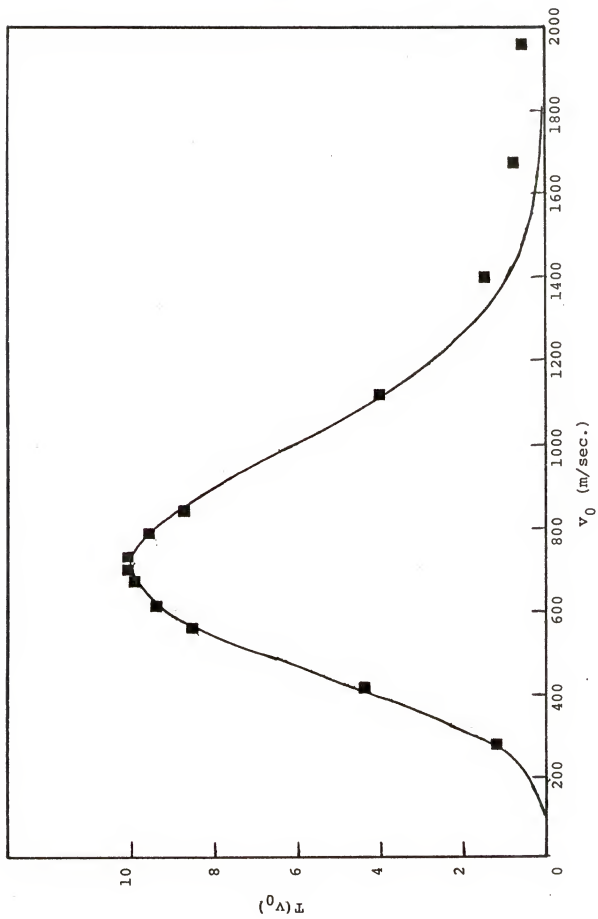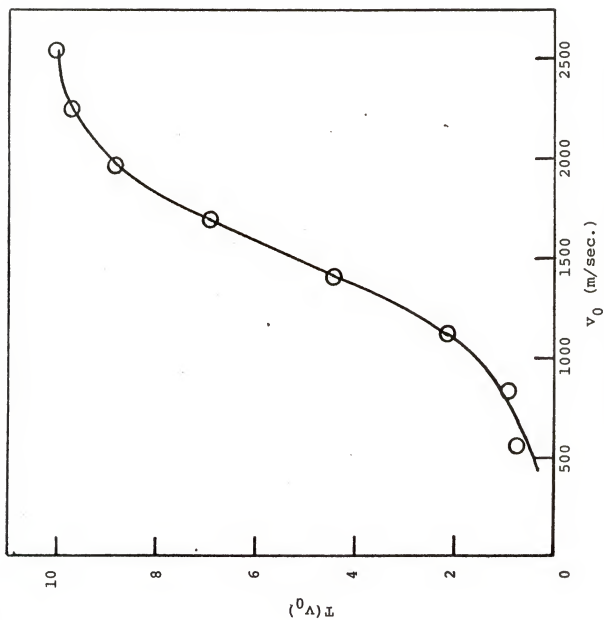
Figure 22. Helium $T(v_0)$ Distribution

no problems with the selector (which is a new design for this laboratory), a time-of-flight analysis of the metastable atom beam was undertaken.

The time-of-flight analysis was accomplished by chopping the metastable atom beam at a frequency of 90 hz. using the chopper of figure 13.

It is important in time-of-flight measurements to know accurately the timing relationship of the waveform eductor trigger pulse to the actual production of a beam pulse. It is not sufficient to assume that the triggering pulse corresponds to perfect alignment of the chopper slot with the detected part of the beam. Fortunately, the discharge source provides a convenient way of determining this relationship. The velocity selector discs were removed, and the arrival of light from a helium discharge was detected by the multiplier and compared with the arrival of the waveform eductor triggering pulse. It was found that there were two light peaks (due to the narrow chopper slots being slightly off axis) which arrived 19 µsec. and 36 µsec. after the waveform eductor was triggered. The measured flight times were corrected by subtracting the average of these two numbers (28 µsec.) which amounts to a correction of 15% in the least favorable case.

Typical time-of-flight peaks for metastable helium and metastable argon are shown in figure 23 for a velocity selector (using disc set I) frequency of 300 hz. The intensity

Figure 23. Time-of-Flight Profiles

□ Helium

○ Argon

Selector Frequency = 300 hz.

Relative Density vs Time-of-flight (μsec.)
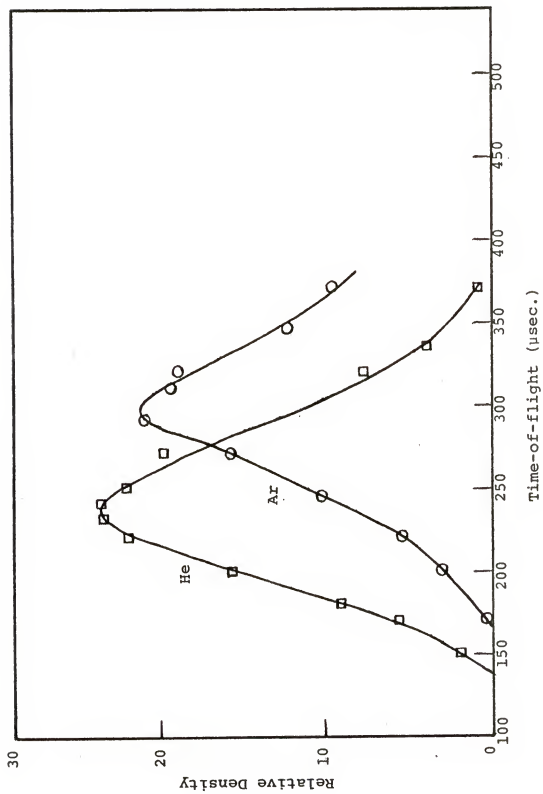
distributions measured by the electron multiplier were converted to density versus time-of-flight plots since the velocity used in equation (9) should correspond to the maximum beam density. The difference in nominal velocities for helium and argon at the same selector frequency is a phenomenon not observed in higher resolution velocity selectors and requires some consideration. It is obvious that, v_0, as defined in Table I, should not be taken as the nominal velocity for this selector because v_0 is a function of the velocity selector parameters only and should not be different for argon and helium. Further evidence of this is shown in figure 24 where the factor λ' relating nominal velocity to velocity selector frequency is plotted against the velocity selector frequency. If the nominal velocity were given by v_0, λ' would be equal to λ and would be independent of frequency. The nominal velocity is given by v_0 only in regions of the distribution where the Maxwell-Boltzmann density distribution function is independent of velocity. For the 2° discs, the relationship between v_0 and the velocity corresponding to maximum intensity is shown in figure 25. The product $I(v) B(v)$ is plotted as a function of velocity for a source temperature of $650^o K$ and a selector frequency of 300 hz. for both helium and argon. It is clear that v_0 (1686 m/sec.) is not the best choice for the nominal argon velocity. The factor $I(v)$ is decreasing very rapidly for argon in the selected velocity range, and the peak is shifted to the low velocity side of v_0. On the other hand, $I(v)$ for helium

Figure 24. Frequency Dependence of λ'

○ Ar, 2° discs
● He, 2° discs
△ Ar, 3° discs
▲ He, 3° discs
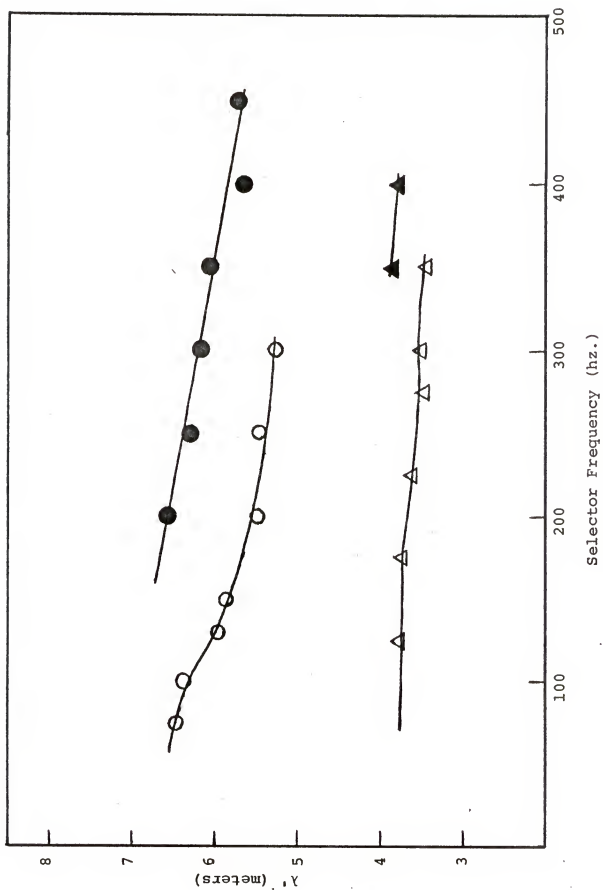
Figure 25. Deviation of Nominal Velocity from v_0
Calculation is for $v_0 = 1686 \text{m/sec.}$ and $T = 650^\circ \text{K.}$

Ar*

He*
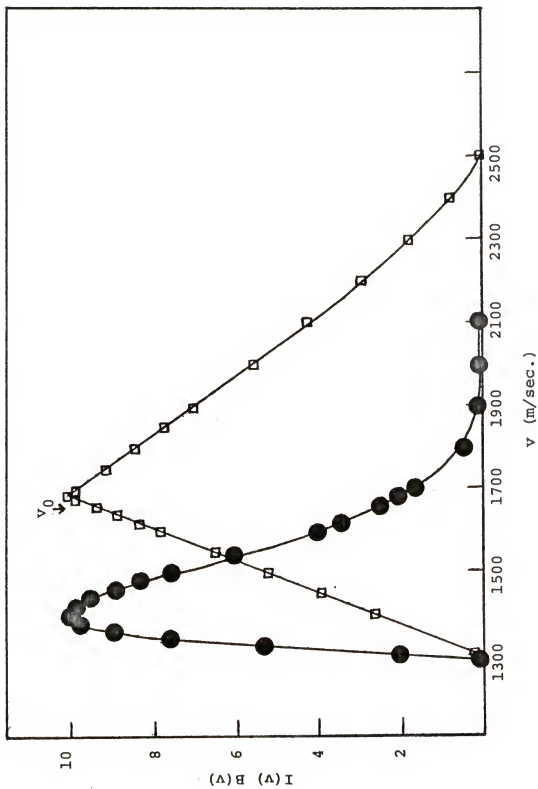
changes only slightly in this range (which includes the maximum value of I(v) at approximately 2000 m/sec.) so that the triangular function B(v) dominates and v_0 corresponds to the velocity at the peak. The difference in the peaks for argon and helium corresponds to a difference in flight time of 55 μsec. which agrees well with the experimentally observed difference of 61 μsec. (see figure 23). The variation of λ' with frequency is due to the "skewing" effect described above which depends on the portion of I(v) being sampled by the selector. Figure 24 also presents the results of time-of-flight analysis of the 3° discs (set II). The same effects are present with these discs, but to a lesser extent due to the improved resolution.

From this analysis it was concluded that metastable atom beam velocities calculated from time-of-flight should be used in cross section and relative energy calcuations.

C. Characterization of the Nozzle Beam

Measurements of the variation of relative nitrogen beam intensity with nozzle-skimmer distance at a source pressure of 923 torr are shown in figure 26. The beam is attenuated at small distances by skimmer interference and at large distances by collisions with background gas between nozzle and skimmer.[94] It was found that a nozzle skimmer distance of 0.45" produced a greater photon flux (due to the larger intersection volume) than the nozzle-skimmer distance (0.65") which produced the maximum nitrogen beam intensity. At
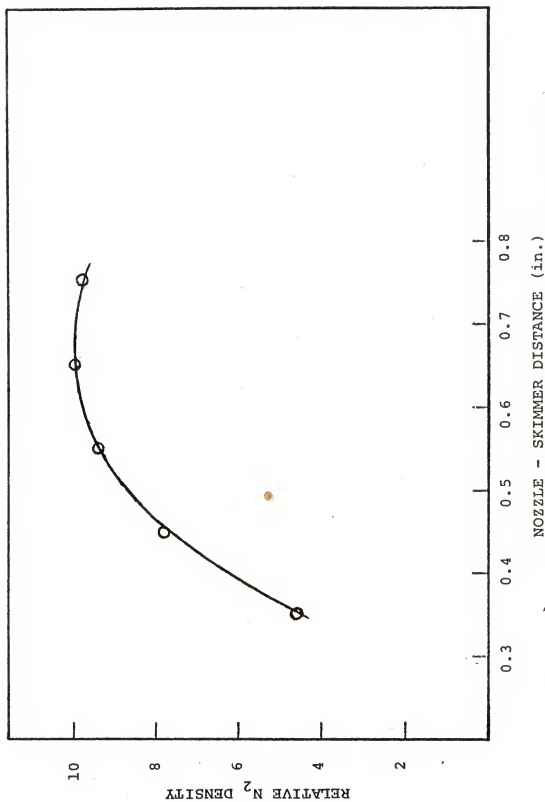
Figure 26. Effect of Nozzle - Skimmer Distance on Beam Density

distances less than 0.45", the main chamber pressure rose rapidly, and the metastable atom beam was attenuated. Therefore, 0.45" was chosen for the nozzle skimmer distance used in these studies. At the oven pressures of approximately 900 torr used, the main chamber pressure was 6×10^{-6} torr, and the nozzle chamber pressure was $3-4 \times 10^{-4}$ torr.

The velocity profile of the nozzle beam was measured as described in section IIF. The timing relationship between beam pulse production and waveform eductor triggering was determined by simulating the nozzle beam with a laser beam. For this purpose, the nozzle cap was replaced by a photocell located in the exact position as the nozzle orifice. The laser beam was directed through the ionizer entrance slit, collimator, and skimmer onto the photocell. Pulses from the photocell (corresponding to beam pulses) preceded the triggering pulses by 12 μsec. and the appropriate corrections to the flight time were made. Another correction was made for the approximately 8 μsec. required for ions to pass from the ionizer to the electron multiplier.

The parameter which is most often used to characterize nozzle beams is the effective Mach number M_S at the skimmer entrance which is related to the more relevant speed ratio S_S by $S_S = (\frac{\gamma}{2})^{1/2} M_S$. The effective Mach number may be obtained experimentally using equation (26) by inserting various values of M_S and comparing the calculated distribution to the experimentally measured one. In order to estimate the value of M_S, the approximate relationship[95] between the velocity

resolution and M_S was used:

$$\frac{\Delta v}{v} \simeq \frac{1.8}{M_S}$$

where Δv is the full width at half-maximum (FWHM) of the distribution and v is the nominal velocity. It will be shown in the next section that $\Delta v/v$ for the pure nitrogen beam under the experimental conditions is 0.19 so that the approximate Mach number is 9.5. In order to determine the Mach number more accurately, the relative intensity was plotted against relative time-of-flight according to equation (26) for M_S values of 9, 10, and 11. The results are shown in figure 27 along with the experimentally determined distribution. The distribution with a Mach number of 10 best fits the experimental data. The corresponding speed ratio is 8.4.

A complete expansion in which the entire enthalpy is converted into directed translational motion would produce a beam with translational energy given by equation (25). For nitrogen at room temperature T_0, $C_p \approx \frac{7k}{2}$, $E_z = \frac{7k\ T_0}{2}$, and $v = (\frac{7k\ T_0}{m})^{1/2}$ = 787 m/sec. Experimentally determined nominal velocities for the pure nitrogen beam varied from 765 to 787 m/sec. so that expansion is very nearly complete. An estimate of the amount of cooling which occurs upon expansion may be obtained from the relation

$$T/T_0 = (1 - \frac{\gamma-1}{2}\ M_S{}^2)^{-1}$$

where T is a temperature which is associated with the remaining internal and random translational energy after expansion. For $\gamma = 7/5$ and $M_S = 10$, this beam "temperature" is found

Figure 27. Relative Time of Flight Distributions

● Experimentally determined distribution

- - - Calculated distribution for M = 9

——— Calculated distribution for M = 10

-·- Calculated distribution for M = 11

高
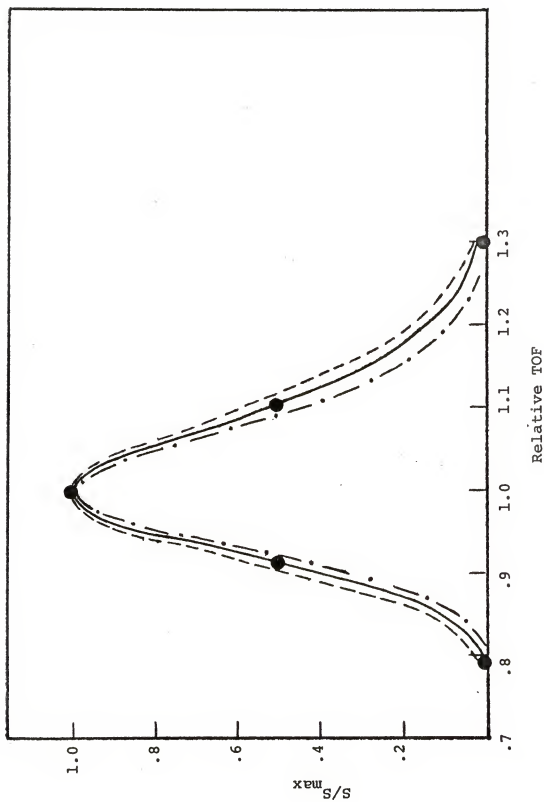
to be 15°K. Calculation of translational beam energy using $E_z = C_p(T_0-T)$ predicts a bulk stream velocity of 767 m/sec. which is in the range of experimentally observed nominal velocities.

The effect of seeding the nitrogen beam with various amounts of helium is that the nominal velocity may be increased continuously to a velocity of approximately twice that of the unseeded beam before the nitrogen density becomes too small to produce a measurable photon flux. This is accomplished with slightly improved resolution over the unseeded beam. This is discussed further in section IIIE. Typical nominal velocities achieved by seeding and the effect on nitrogen beam density in the intersection zone are shown below:

Time-of-flight (μsec.)	nominal velocity (m/sec.)	rel. N_2 density
1	694	776	1.00
2	598	900	1.05
3	466	1155	0.67
4	378	1424	0.25

The relative densities were calculated from the normalization procedure described in section VB. Beam condition 1 is a pure nitrogen beam at an oven pressure of 900 torr. The seeded beams tabulated above are characterized by the total oven pressure P and the nitrogen flow rate F:

	P(PSI)	F (standard cm^3/min.)
2	14.0	27.5
3	10.2	10.5
4	10.3	3.6

D. Accessible Velocity and Energy Ranges

The velocity selector described in section IID has a frequency range of 75 - 450 hz. At lower frequencies the discs do not straighten out properly, and, above 450 hz., the bearings heat up extremely rapidly. Using the 2° velocity selector discs, the range of v_0 is 422 - 2529 m/sec. Due to the variation of λ' with frequency, the accessible nominal velocity range differs from the v_0 range. For instance, with argon under typical source conditions, the lowest accessible argon nominal velocity is 484 m/sec. This range of v_0 includes the peak of the argon $T(v_0)$ distribution at 127 hz. where $v_0 = 714$ m/sec. (see figure 21). The 3° discs sample a v_0 range of 271 - 1625 m/sec. which includes practically all of the argon $T(v_0)$ distribution. The peak is found at a frequency of about 200 hz. Except for the very low energy measurements, the 2° discs were used instead of the 3° discs for the $Ar*/N_2$ measurements because they allow the selector to be run at lower frequencies prolonging the lifetime of the bearings.

The portion of the helium $T(v_0)$ distribution which is accessible is much more limited. With the 2° discs, the peak of the helium distribution is almost reached, but the higher velocity part (where the intensity would be expected to remain high over a considerable range) cannot be used.

The energy range of the $Ar*/N_2$ experiment is limited on the low energy end by the minimum nitrogen nominal velocity (780 m/sec.) possible and the minimum argon nominal velocity

(300 m/sec.). These correspond to a relative velocity of
840 m/sec. and a relative energy of 0.060 eV. At the high
energy end, the range is limited by the rapidly decreasing
photon signal with increasing energy, as both beam densities
decrease. The argon beam density decreases because the
velocity selector is sampling the argon $T(v_0)$ distribution
at large velocities (1334 m/sec. for the maximum argon
nominal velocity used) and the nitrogen beam density decreases
as larger percentages of helium are added to the beam. The
maximum nitrogen velocity used was 1433 m/sec. so that the
maximum relative velocity and relative energy were 1958 m/sec.
and 0.327 eV., respectively.

The energy range of the He*/N_2 experiment is limited on
the low energy end by the low helium beam density. The mini-
mum helium nominal velocity used (1020 m/sec.) corresponds to
the lowest beam density which still results in a measurable
photon flux when interacting with a pure nitrogen beam with a
nominal velocity of 780 m/sec. The corresponding relative
velocity and relative energy are 1280 m/sec. and 0.030 eV.
At the high energy end, the range is limited by the maximum
velocity selector frequency possible (450 hz. corresponding
to a helium nominal velocity of 2570 m/sec.). Seeding the
nozzle beam is not nearly as effective a means of extending
the range to higher energies as it is for the Ar*/N_2 experiment,
because the relative velocity is dominated by the higher
velocity helium beam. The maximum nitrogen nominal velocity

used (1410 m/sec.) allowed a maximum relative velocity of 2933 m/sec. and a maximum relative energy of 0.157 eV. This is only 0.02 eV. greater than the maximum energy obtained with a pure nitrogen beam.

E. Velocity and Energy Resolution Calculations

The relative velocity resolution of this experiment may be expressed in terms of the variance $\sigma^2(v_r)$:

$$\sigma^2(v_r) = \sigma_A^2 (\frac{dv_r}{dv_A})^2 + \sigma_B^2 (\frac{dv_r}{dv_B})^2$$

where $v_r = (v_A^2 + v_B^2)^{1/2}$ is the relative velocity, σ_A^2 is the velocity variance of beam A, and σ_B^2 is the velocity variance of beam B. Since $dv_r/dv_A = v_A/v_r$ and $dv_r/dv_B = v_B/v_r$,

$$\sigma(v_r) = \frac{1}{v_r}[\sigma_A^2 v_A^2 + \sigma_B^2 v_B^2]^{1/2}. \qquad (27)$$

Since it is easier to measure the half-widths of velocity distributions than it is to determine the standard deviations, equation (27) is re-written as

$$\Delta v_r = \frac{1}{v_r}[(\Delta v_A)^2 v_A^2 + (\Delta v_B)^2 v_B^2]^{1/2}$$

where Δv_r, Δv_A, and Δv_B are the half-widths of the distributions. For Gaussian distributions, the half-width is 2.354 times the standard deviation. The relative velocity resolution $w(v_r)$ is given by

$$w(v_r) = \frac{\Delta v_r}{v_r} = \frac{1}{v_r^2}[(\Delta v_A)^2 v_A^2 + (\Delta v_B)^2 v_B^2]^{1/2}$$

or, in terms of the resolutions $w_A = \frac{\Delta v_A}{v_A}$ and $w_B = \frac{\Delta v_B}{v_B}$:

$$w(v_r) = \frac{1}{v_r^2}[w_A^2 v_A^4 + w_B^2 v_B^4]^{1/2} \qquad (28)$$

The relative energy resolution $w(E_r)$ is related to $w(v_r)$ by $w(E_r) = 2 \, w(v_r)$.

From Table I it is seen that the velocity selector resolution is constant for a particular set of discs. This resolution corresponds to $\dfrac{v_{max} - v_{min}}{2v_0}$, and $(v_{max} - v_{min})/2$ is equal to the half-width for triangular distributions; that is, when the distribution is dominated by the slit function. The resolution as defined by the selector parameters will deviate slightly from the resolution calculated from the half-width for non-triangular distributions. Values of the resolution calculated from the time-of-flight profiles are preferable; however, many of the time-of-flight measurements for the metastable atom beam were made under conditions in which the half-width was severely broadened due to background. Measurements made under favorable conditions of intensity produced resolutions close to the values of 0.36 and 0.21 expected for discs I and II, respectively. Therefore, these values for the metastable atom beam resolution were used in the relative velocity resolution calculations.

The results for the four nozzle beam conditions used are shown in Table IV for Ar^*/N_2 and the 2° selector discs (set I). The resolution is better at the larger nitrogen and smaller argon beam velocities where the poor argon beam resolution is less important. The results for the 3° discs on this same system are shown in Table V. The argon beam resolution is comparable to the nozzle beam resolution so that $w(v_r)$ is

TABLE IV

Resolution Parameters for Ar* + N_2 (2° Discs)

v_{N_2} (m/sec)	v_{Ar} (m/sec)	v_r (m/sec)	E_r (eV.)	w_{N_2}	w_{Ar}	$w(v_r)$	$w(E_r)$
776	1350	1557	0.207	0.19	0.36	0.27	0.54
776	1078	1328	0.150	0.19	0.36	0.25	0.50
776	875	1169	0.117	0.19	0.36	0.22	0.44
776	626	997	0.085	0.19	0.36	0.18	0.36
776	475	910	0.071	0.19	0.36	0.17	0.34
900	1350	1622	0.225	0.16	0.36	0.25	0.50
900	1078	1404	0.168	0.16	0.36	0.22	0.44
900	875	1255	0.134	0.16	0.36	0.19	0.38
900	626	1096	0.103	0.16	0.36	0.16	0.32
900	475	1018	0.088	0.16	0.36	0.15	0.30
1155	1350	1777	0.269	0.16	0.36	0.22	0.44
1155	1078	1580	0.213	0.16	0.36	0.19	0.38
1155	875	1449	0.179	0.16	0.36	0.17	0.34

TABLE IV - continued

v_{N_2} (m/sec)	v_{Ar} (m/sec)	v_r (m/sec)	E_r (eV.)	w_{N_2}	w_{Ar}	$w(v_r)$	$w(E_r)$
1155	626	1314	0.147	0.16	0.36	0.15	0.30
1155	475	1249	0.133	0.16	0.36	0.15	0.30
1424	1350	1962	0.329	0.16	0.36	0.19	0.38
1424	1078	1786	0.272	0.16	0.36	0.17	0.34
1424	875	1671	0.238	0.16	0.36	0.15	0.30
1424	626	1556	0.206	0.16	0.36	0.15	0.30
1424	475	1501	0.192	0.16	0.36	0.15	0.30

TABLE V

Resolution Parameters for Ar* + N_2 ($3°$ Discs)

v_{N_2} (m/sec)	v_{Ar} (m/sec)	v_r (m/sec)	E_r (eV.)	w_{N_2}	w_{Ar}	$w(V_r)$	$w(E_r)$
776	944	1222	0.127	0.19	0.21	0.15	0.30
776	814	1125	0.108	0.19	0.21	0.14	0.28
776	653	1014	0.088	0.19	0.21	0.14	0.28
776	466	905	0.070	0.19	0.21	0.15	0.30
776	352	852	0.062	0.19	0.21	0.16	0.32

approximately constant over the whole range in which these discs were used.

The results for He*/N_2 and the 2^O discs are presented in Table VI. The resolution is slightly worse due to domination by the faster (and more poorly resolved) helium beam.

In summary, the relative velocity resolution behaves in a rather complicated way over the energy ranges studied. The resolution is best for Ar*/N_2 at the very low energies (where the 3° discs are used). For a particular nozzle beam condition, the resolution with the 2^O discs is best at the lower energies (where the slow argon beam is less important), but the resolution improves with increasing energy when the energy increase is due to a faster nozzle beam. The same comments apply to the He*/N_2 system except that the low energy results were obtained with the 2^O discs and, therefore, are more poorly resolved than the low energy Ar*/N_2 results.

TABLE VI

Resolution Parameters for He* + N_2 (2° Discs)

v_{N_2}(m/sec)	v_{He}(m/sec)	v_r(m/sec)	E_r(eV.)	w_{N_2}	w_{He}	$w(v_r)$	$w(E_r)$
773	2500	2617	0.124	0.19	0.36	0.33	0.66
773	2275	2403	0.105	0.19	0.36	0.32	0.64
773	2198	2330	0.098	0.19	0.36	0.32	0.64
773	1896	2048	0.078	0.19	0.36	0.31	0.62
773	1585	1763	0.056	0.19	0.36	0.29	0.58
773	1350	1556	0.044	0.19	0.36	0.28	0.56
1406	2500	2868	0.149	0.16	0.36	0.28	0.56
1406	2275	2674	0.130	0.16	0.36	0.26	0.52
1406	1298	2609	0.123	0.16	0.36	0.26	0.52
1406	1896	2330	0.101	0.16	0.36	0.24	0.48
1406	1585	2119	0.081	0.16	0.36	0.21	0.42
1406	1350	1949	0.069	0.16	0.36	0.19	0.38

CHAPTER IV

EXPERIMENTAL PROCEDURE FOR CROSS SECTION MEASUREMENTS

A. Optical Considerations for Ar*/N_2

The optical spectra observed in flowing afterglow measurements are useful in designing the experiments described here. Stedman and Setser[96] and Setser et al.[97] studied the Ar($^3P_{2,0}$)/N_2 system and observed three emission bands:

$$C^3\Pi_u \to B^3\Pi_g \qquad 2^{nd} \text{ positive}$$
$$B^3\Pi_g \to A^3\Sigma_u^+ \qquad 1^{st} \text{ positive}$$
$$A^3\Sigma_u^+ \to X^1\Sigma_g^+ \qquad \text{Vegard-Kaplan}$$

Relevant potential energy curves[98] for N_2 and N_2^+ are shown in figure 28. The $A^3\Sigma_u^+$ is a metastable state and the A → X transition was only observed at times ≥ 50msec. downstream from the mixing zone in flowing afterglow studies and therefore is not observed in the present experiment. The B → A transition occurs over a wide range of wavelengths greater than 5000 Å, the most intense band being the (0,0) band at 10510 Å. Therefore, the most intense transitions are not detected at all by the apparatus of this study, and the few that are observed are detected with very low sensitivity (see figure 20). Additionally, the lifetime of the B excited states depends strongly on the particular vibrational transition, and some of these lifetimes are relatively long. An average lifetime of the B state is 7 μsec.[99] which corresponds to a
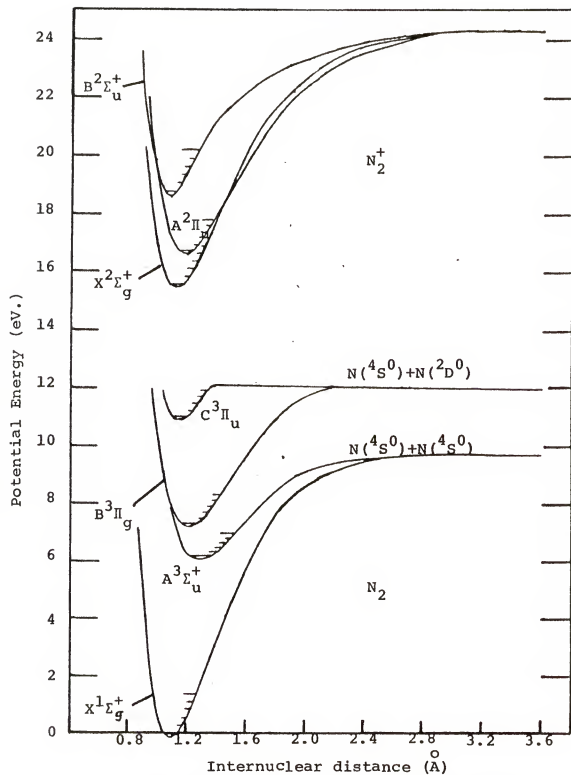
Figure 28. Nitrogen Potential Curves

movement from the point of excitation of 0.6 to 1.2 cm, de-
pending on the nitrogen velocity, before fluorescence occurs.
Transitions to the higher A vibrational levels are even
slower, and a significant portion of the fluorescence may
be lost. The $C^3\Pi_u \rightarrow B^3\Pi_g$ transition was observed in flowing
afterglow studies over the wavelength range 3100-4100 Å with
the most intense transition (0,0) at 3371 Å. These transition
occur in the range where our photomultiplier sensitivity is
greatest. The approximate lifetime for the C → B transition
is 50 nsec. so that all the fluorescence occurs in the inter-
section zone.

In order to observe the relative contributions of the
C → B and B → A transitions to the photon flux, a cut-off
filter[100] was used to eliminate transitions at $\lambda \leq 5000$ Å.
In this way it was determined that the B → A signal was about
5% of the C→B signal and remained nearly constant over the
entire energy range studied. Additionally, the relative cross
section as a function of relative translational energy was
determined over a limited energy range using a pure nitrogen
target beam with a cut-off filter[83c] which eliminated transi-
tions at $\lambda \geq 4750$ Å. This experiment, compared with results
obtained with no filter, confirmed the approximately constant
5% B → A contribution. Since better counting statistics were
obtained with no filter, the Ar*(C)/N_2 cross section measure-
ments were obtained without a filter. The signal observed
from the B → A transition was too small to permit accurate
measurements due to the reasons mentioned above.

Consideration must be given to possible errors caused by the variation of detection efficiency with wavelength. This is a problem only if the relative vibrational energy level populations $I_{v'}$ change with relative collision energy. Table VII lists the principal C → B transitions for the lower C state vibrational levels, the corresponding wavelengths, the Franck-Condon factors[101] associated with the transitions, and the detection efficiency. The latter is the product of the cathode quantum efficiency and the lens transmission of the optical system. Significant errors may arise if, for instance, the population of the $v' = 1$ level increased at the expense of the $v' = 0$ level. Then, some of the light which had been emitted from $v' = 0$ and detected at relatively high efficiency, is emitted at 3159 Å where the detection efficiency is lower. The cross section will thus appear to decrease even if there is no change in the overall population of the electronic state. However, the relative vibrational level populations I_0: I_1: I_2 were found to be 100: 18: 2.5 at 300°K and 100: 20: 3 at 77°K in flowing afterglow studies.[96] Therefore, the relative vibrational energy level populations are not very sensitive to collision energy, and errors due to the wavelength response of the detection system should be small.

The photon count rates due to velocity selected interactions of Ar* with N_2, background count rates, and required observation times for the relative standard deviations

TABLE VII

Optical System Response To $N_2(C) \rightarrow N_2(B)$ Transitions

v'	v"	$\lambda (\overset{\circ}{A})$	FC[a]	DE(%)[b]
0	0	3371	0.45	14
0	1	3577	0.33	15
0	2	3805	0.15	18
0	3	4059	0.05	19
1	0	3159	0.39	5
1	2	3537	0.20	15
1	3	3756	0.20	18
1	4	3998	0.11	19
1	5	4270	0.05	18
2	0	2977	0.13	1
2	1	3136	0.32	5
2	3	3500	0.06	15
2	4	3711	0.16	17
2	5	3943	0.14	19
2	6	4200	0.083	18
3	1	2962	0.25	1
3	2	3117	0.16	3
3	3	3285	0.12	9
3	5	3672	0.089	18
3	6	3895	0.14	19

TABLE VII - continued

v'	v"	λ (Å)	FC[a]	DE(%)[b]
3	7	4142	0.11	18
3	8	4417	0.06	17

[a] FC Franck Condon factors

[b] DE Detection efficiency

achieved are listed in Table VIII for some typical beam
conditions. The primary contribution to background noise is
from reflected light escaping the discharge chamber and find-
ing its way to the photomultiplier, but there are also con-
tributions from photomultiplier dark noise (about 10 counts
per second), and non-velocity selected interactions of Ar*
with background nitrogen molecules.

B. Optical Considerations for He*/N_2

Richardson and Setser[102] have observed the optical
spectra due to metastable helium atom interactions with
nitrogen in a flow tube. This system has also been studied
by Hotop and Niehaus[18b] using Penning electron spectroscopy.
These studies show that N_2^+ is produced in the $X^2\Sigma_g^+$, $A^2\Pi_u$,
and $B^2\Sigma_u^+$ states. The optical spectra consist of two emission
bands, $B \rightarrow X$ and $A \rightarrow X$. No emissions from excited molecular
states of N_2 were observed. The B state vibrational levels
populated are v' = 0 and 1 with observed relative populations
$I_0: I_1$ of 100: 18 ± 3[18b] and 100: 12 ± 4.[102] The principal
$B \rightarrow X$ transitions observed were between 3580 and 4280 $\overset{\circ}{A}$ and
the approximate lifetime of this transition is 60 nsec.
$A \rightarrow X$ transitions observed in the flowing afterglow measure-
ments were between 6000 and 8000 $\overset{\circ}{A}$. Thus, the comments
above pertaining to $N_2(B \rightarrow A)$ transitions apply to $N_2^+(A \rightarrow X)$
transitions; i.e., they occur in a region of low detector
sensitivity for this apparatus.

The relative contributions of the $B \rightarrow X$ and $A \rightarrow X$ tran-
sitions to the detected photon signal were determined by

TABLE VIII

Typical Photon Count Rates For Ar*/N$_2$

n_{N_2}	I_{Ar^*} (mV.)	E_{rel}	Background (sec^{-1})	Signal (sec^{-1})	Observation time (sec)	r.s.d.
1.00	208	0.11	150	50	600	1.8%
1.00	88	0.18	125	17	1440	2.2%
0.67	212	0.17	118	36	680	2.1%
0.67	104	0.23	93	13	1960	2.3%
0.25	213	0.22	95	18	760	2.3%
0.25	78	0.31	83	3	3720	5.0%

using the filter which blocks all emissions at wavelengths
less than 5000 Å. Preliminary measurements with and without
this filter indicated an A → X contribution to the photon
signal of approximately 30% of the total photon signal at
low collision energies (0.03 eV.). The A → X contribution
decreased with increasing collision energy and was negligible
at 0.10 eV. Since the principal A → X transitions are detected
with very low efficiency (or not at all) in a range where
the detection efficiency changes rapidly, no attempt was made
to measure accurately the energy dependence of the relative
cross section for production of $N_2^+(A^2\Pi_u)$.

The principal transitions from the $N_2^+(B, v' = 0,1)$
states are listed in Table IX along with corresponding
wavelengths, Franck-Condon factors and detection efficiencies.
The detection efficiencies include the effects of the filter
which blocks all wavelengths greater than 4750 Å and there-
fore eliminates the A → X transition. This filter was used
in all measurements of the relative cross section for pro-
duction of $N_2^+(B^2\Sigma_u^+)$. Again, detector wavelength response
should not have a large effect since the relative vibrational
level populations are insensitive to collision energy.[102]

Typical count rates due to state selected metastable
helium collisions with nitrogen, background count rates, and
required observation times are listed in Table X.

TABLE IX

Optical System Response To $N_2^+(B) \rightarrow N_2^+(X)$ Transitions

v'	v"	λ (Å)	FC[a]	DE(%)[b]
0	0	3914	0.65	15
0	1	4278	0.26	15
0	2	4709	0.070	13
1	0	3583	0.30	12
1	1	3884	0.22	15
1	2	4237	0.29	15
1	3	4652	0.13	14
2	1	3564	0.41	12
2	2	3858	0.05	15
2	3	4199	0.23	15
2	4	4600	0.17	14
2	5	5077	0.071	0

[a] FC Franck Condon factors

[b] DE Detection efficiency

TABLE X

Typical Photon Count Rates For He*/N_2

n_{N_2}	I_{He*} (mV.)	E_{rel}	Background (sec^{-1})	Signal (sec^{-1})	Observation time (sec)	r.s.d.
1.00	270	0.13	55	19	240	4.2%
1.00	48	0.04	20	2	1560	10%
0.40	235	0.157	28	8	280	7%
0.40	185	0.115	25	6	400	4%

C. Experimental Procedure

The cross section measurements are begun by establishing a steady nozzle beam flow rate. For a pure nitrogen beam, this is accomplished as described in section IIB, and a steady nozzle beam intensity is achieved rapidly as measured by the mass spectrometer. For seeded beams, the equilibration time is greater, and oscillations in the nozzle beam intensity and time-of-flight may occur for as long as three hours. Careful adjustment of the leak valves admitting the two beam gases to the inlet manifold alleviates the problem to some extent, but it is necessary to wait at least an hour for the mass flow meter readings, lock-in amplifier signal, and time-of-flight measurements to become constant. When this situation is reached, the nominal time-of-flight is recorded as well as the half-width, and the ionizer is turned off. This is done because of the large contribution of the ionizer filament light emission to the background count rate (about 10^6 counts/second). The flow rates of the beam components are monitored during the experiment to insure constant beam conditions.

The metastable atom beam is produced under the conditions described in section IIC. The intensity distribution $T(v_0)$ is then obtained by scanning the velocity selector frequency over the appropriate range in order to insure that the selector functions properly. This procedure is particularly necessary if the velocity selector discs have been removed

since the last time the distribution was checked. It was
found for the 2^O discs, that very slight changes in disc
alignment can occur in the process of lubricating the
bearings. A significant effect on the observed intensity
distribution results due to a change in the effective helix
angle. For example, the peak valve of $T(v_0)$ varied over a
frequency range of 127-140 hz. under similar argon source
conditions for this reason. The metastable beam time-of-
flight analysis was carried out with an effective helix angle
which gave a $T(v_0)$ peak at 127 hz. and this was used as a
reference distribution. Distributions measured immediately
prior to cross section measurements which were slightly dif-
ferent from this reference distribution were corrected by a
factor which altered the velocity of argon used in equation
(9) by a small amount, no greater than 10%. Energy dependent
cross section measurements made with argon beams that peaked
at 140 hz. agreed well with those made with argon beams
which had peak intensities at 127 hz. after the appropriate
correction was made. All measurements with helium as the
discharge gas were made with the same $T(v_0)$ distribution that
was obtained immediately prior to the time-of-flight analysis,
and no corrections were necessary. The 3° discs were not
subject to critical alignment requirements and the intensity
distributions using these discs were very reproducible.

After the intensity distribution is obtained for a
metastable atom beam which has a steady intensity as measured

by the Faraday cup, photon counting is begun. The dual channel photon counter accumulates signal plus background and background counts for 4 msec. out of each 10 msec. chopping period. After 10^4 cycles (100 sec.), the tele-type prints out these accumulated counts which correspond to 40 seconds for measurement of the desired fluorescent signal. The metastable beam intensity is also printed. The nozzle beam density is not actually measured during the experiment, but is held constant by maintaining constant flow rates and total pressure. The target beam density at the ionizer is not a particularly useful quantity since changes in the beam geometry upon seeding can cause changes in density or volume of the intersection zone. More specif-ically, greater density along the beam axis for a seeded beam relative to the axial density of an unseeded beam would cause a greater mass spectrometer signal for the seeded beam even if the average densities in the intersection zone were equal. Therefore, the nozzle beam density is assumed to be unity until normalization is accomplished as described in Chapter VA.

Every 100 sec., the photon signal S_p and metastable beam intensity are recorded. This is continued until suit-able statistics are obtained. Then the nozzle beam time-of-flight profile is re-measured to insure that the nozzle con-ditions have remained constant. The nominal flight times measured before and after photon counting always agreed to within ± 2 µsec. Then, the velocity selector frequency is

changed and the process is repeated at a different relative velocity. The widest energy range possible is spanned with the particular selector discs used and the given nozzle beam condition. Then, a new nozzle beam nominal velocity is established which, given the relative energy range possible by variation of the metastable atom beam velocity through its accessible spectrum, allows relative energy overlap with the results just obtained. This process is continued until the accessible relative energy range has been covered.

In order to insure against any errors due to unequal counting times in the dual channel counter or any other effects which may bias the experiment, it is customary to shut off the nitrogen flow, pump out the nozzle oven, and measure the photon flux under conditions otherwise identical to those during the actual cross section measurement. In this way it was determined that there was a slight bias in favor of the signal plus background channel which amounted to 0.40 counts/sec. with no filter and 0.10 counts per sec. with the cut-off filter used in the He^*/N_2 experiment. The appropriate corrections were made to the signal count rates. This bias is due to light (chopped at the target beam modulation frequency) from the light emitting diode on the nozzle beam chopper mount.

CHAPTER V

DATA ANALYSIS AND RESULTS

A. Data Analysis

A calculator [93] program was written with three pur-
poses in mind: to aid in determining when sufficient data
had been obtained, to calculate the relative cross sections
and relative translational energies, and to calculate the
uncertainty in the cross sections. The nominal target beam
velocity is calculated and printed from the time-of-flight
input, the metastable atom beam velocity is calculated and
printed from the velocity selector frequency input, the
relative velocity and energy are computed and printed, the
electrometer range setting is entered and stored for later
metastable atom beam intensity calculation. No information
about nozzle beam density is entered since this relative
density is determined by normalization.

As described in section IVE, the signal-averaged photon
count and relative metastable atom beam intensity are re-
corded once every 100 seconds. The metastable atom beam
intensity is in the form of a digital voltmeter signal
which is later converted by the program to the correct
electrometer reading in millivolts. For very low photon
count rates longer counting periods are employed to reduce

113

the amount of data which has to be manually transferred from the teletype to the calculator. From the previous inputs described above and from the new photon and meta- stable intensity inputs, the relative cross section σ_n for each counting period n is calculated from equation (9). After at least two such cross sections are calculated, the standard deviation of the mean cross section (equal to s.d./$\sqrt{n}$ where s.d. is the standard deviation), and the relative standard deviation, r.s.d., of the mean are cal- culated and printed. Measurements are continued until the desired r.s.d. is reached. For the Ar^*/N_2 experiment, r.s.d. = 3% was the goal for cross section precision, but this re- quirement was relaxed considerably in order to extend the results to higher relative energies. For the He^*/N_2 experi- ment, r.s.d. = 5% was the goal, but this requirement was relaxed at both the upper and lower ends of the energy range.

The data obtained in this way were later re-calculated using the metastable atom beam velocities measured by time- of-flight, the nozzle beam velocities corrected as described in section IIIC, and the photon signals corrected for the bias described in section IVC.

The error bars for the results presented in the next section represent approximately ± the standard deviation of the mean cross section.

B. Results of Relative Cross Section Measurements

Measurements of the cross section for production of
$N_2(C)$ in collision of $N_2(X)$ with $Ar(^3P_{2,0})$ corresponding
to six different nozzle beam conditions are shown in figure
29. The relative cross section in arbitrary units is plotted
versus relative translational energy. In the critial areas
at low energies, where the cross section changes rapidly,
there is considerable overlap of the results for different
target beams to permit accurate normalization. The shapes
of the cross section curves agree well in the overlap
regions.

Each curve of figure 28 was multiplied by the factor
which brings it into agreement with a reference curve.
The reference curve begins with the results of the unseeded
nozzle beam (nominal velocity of 765 m/sec.) and 2^O velocity
selector discs. The curve corresponding to a nominal
nitrogen velocity of 776 m/sec. and 3° discs was normalized
to the first curve in a region where both curves exhibit
low cross section uncertainties, and these two curves formed
the new reference curve. Similarly, the results correspond-
ing to 775, 900, 1155, and 1424 m/sec. were normalized to
the reference curve in that order. The normalization factors
represent relative nitrogen beam densities.

The results are shown in figure 30. The cross section
rises rapidly from 0.06 eV. to a maximum at 0.12 eV. and
gradually decreases from the that point to 0.36 eV.

Figure 29. Unnormalized Ar*/N$_2$ Cross Sections

	Nominal N$_2$ Velocity	Selector Discs
●	775 m sec.	2°
■	776 m/sec.	3°
◄	765 m/sec.	2°
○	900 m/sec.	2°
△	1155 m/sec.	2°
□	1424 m/sec.	2°

Relative Energy (eV.)

Relative Cross Section (arb. units)
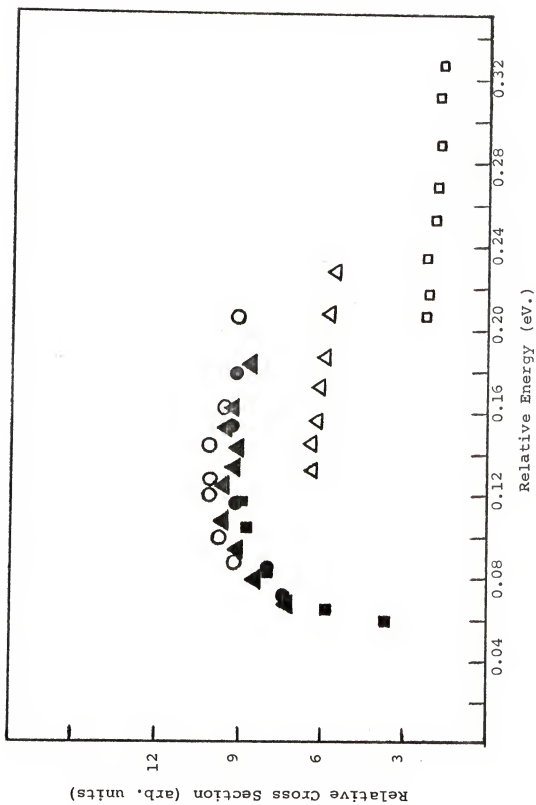
Figure 30. Translational Energy Dependence of the Relative Cross Section – Ar* + N_2 → Ar + N_2(C)

● Results of the present study

——— Results of reference 22

■ Landau-Zener fit at the maximum

$Ar(^3P_{2,0}) + N_2(X^1\Sigma_g^+) \longrightarrow Ar(^1S) + N_2(C^3\Pi_u)$
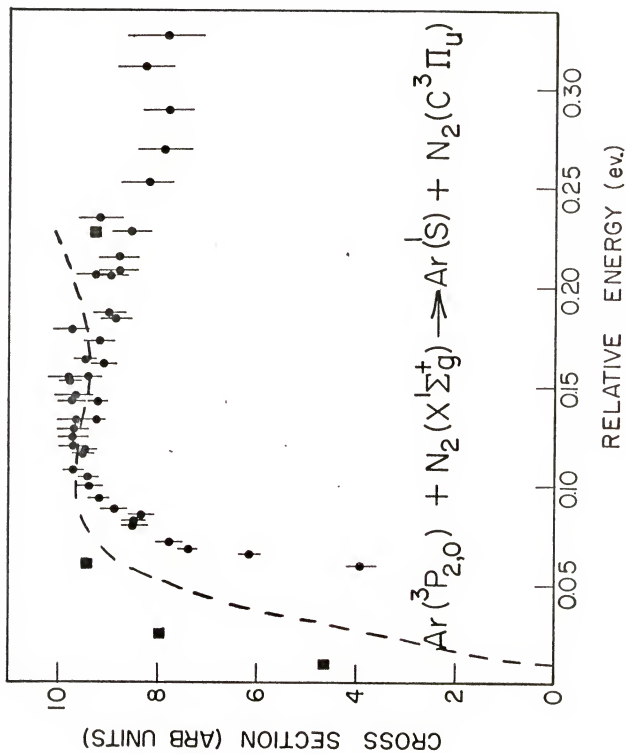
Since the literature value[35] for quenching of Ar* by N_2 corresponds to an energy (0.033 eV) below the lower energy limit of this study, no attempt was made to obtain absolute cross sections by the procedure described in section IC.

Measurements of the cross section σ_B for production of $N_2^+(B)$ in collisions of $N_2(X)$ with $He(2^{1,3}S)$ are shown in figure 31. The data represent measurements with two different nozzle beam conditions normalized to each other in the manner described above. The relative measurements were converted to absolute cross sections by comparison with measurements[16] of the total ionization cross section σ_T of $N_2(X)$ in collisions with $He(2^3S)$ and by using the relative electronic energy level populations from Penning electron spectroscopic[18b] measurements at 300-400°K. The total ionization cross sections were normalized to flowing afterglow results at room temperature using equation (9). The ratio σ_B/σ_T was found to be 0.41. Using a temperature of 350°K the corresponding average relative collision energy is 0.38 eV. At this collision energy σ_T is approximately 3.7 $\overset{\circ}{A}^2$ so that σ_B is 1.5 $\overset{\circ}{A}^2$. The relative cross sections measured in this study were multiplied by the factor which made the cross section equal to 1.5 $\overset{\circ}{A}^2$ at 0.38 eV.

The cross section for production of $N_2^+(B)$ goes through a minimum at approximately 0.04 eV, nearly doubles between 0.04 and 0.10 eV, then increases with gradually decreasing slope.

Figure 31. Translational Energy Dependence of the Relative Cross Section — He* + $N_2(X) \rightarrow$ He + $N_2^+(B)$ + e

$He(2\,^1S, 2\,^3S) + N_2(X\,^1\Sigma_g^+) \longrightarrow He(^1S) + N_2^+(B\,^2\Sigma_u^+) + e$
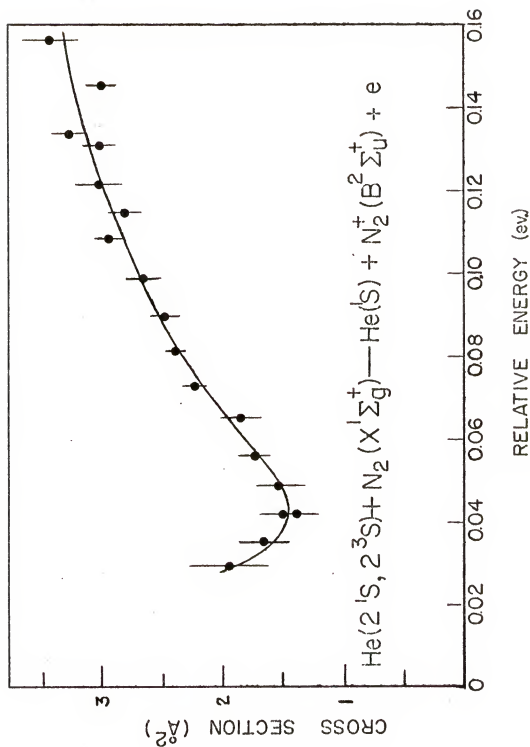
A comparison of the translational energy dependence of σ_T with σ_B is made in figure 32. The total cross section rises almost linearly with increasing relative energy through the range of the present experiment and does so at a rate faster than the increase of σ_B. Thus, the branching ratio σ_B/σ_T decreases with increasing collision energy. This is demonstrated in figure 33 where it is seen that σ_B/σ_T decreases very rapidly at low energies and less rapidly at the higher collision energies.

The absolute cross sections plotted in figure 31 depend on the percentage of singlets in the predominantly 2^3S helium beam of this study, because the normalization is done with respect to the He (2^3S) results of references 16 and 18b. The direction of this effect depends on the relative magnitudes of the total ionization cross sections and on the relative electronic level populations of N_2^+ produced by the two helium states. The He(2^1S) state has a larger total ionization cross section with nitrogen, and, this effect, by itself, would make the absolute results in figure 31 too high by an amount depending on the relative percentages of singlets to triplets in the helium beam. The ratio σ_B/σ_T has not been measured for He(2^1S) + $N_2(X)$. The absolute cross sections are also uncertain due to the wide temperature range reported for the σ_B/σ_T measurement of reference 18b. Average relative collision energies of 0.033 to 0.044 eV.

Figure 32. Total and B State Ionization Cross Sections

σ_T = cross section for total ionization

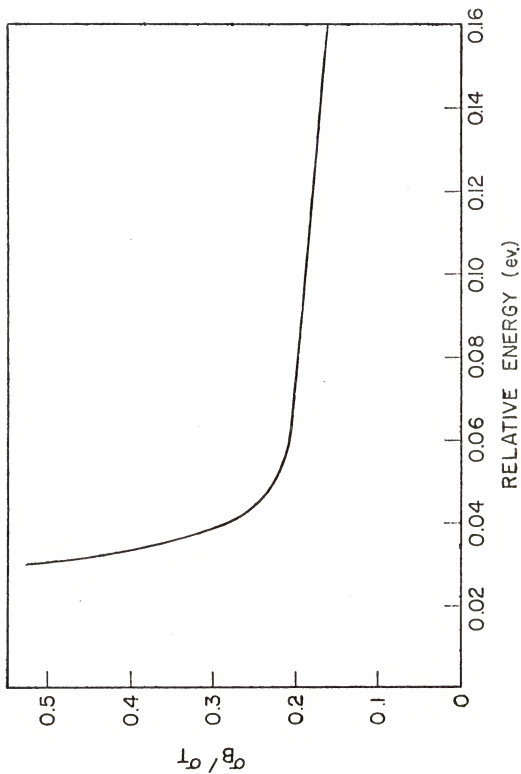σ_B = cross section for ionization to the B state
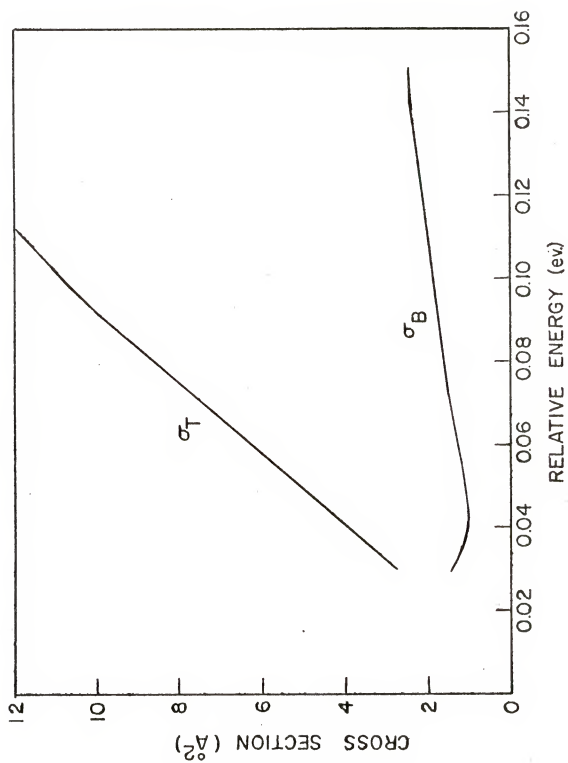
Figure 33. Energy Dependence of the Branching Ratio $\frac{\sigma_B}{\sigma_T}$

are possible, and since this is in the energy range where σ_B/σ_T is changing rapidly, the uncertainty in temperature causes a large uncertainty (about 50%) in σ_B/σ_T.

CHAPTER VI

DISCUSSION

A. <u>Ar* + N$_2$</u>

Lee and Martin[22] have measured the translational
energy dependence of the cross section for the reaction

$$Ar(^3P_{2,0}) + N_2(X^1\Sigma_g^+) \rightarrow Ar(^1S) + N_2(C^3\Pi_u) \qquad (29)$$
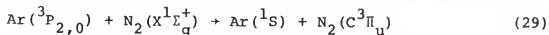
by the time-of-flight (TOF) technique described in section
IB. These results, which are relative cross sections over
the energy range 0.013 eV. to 0.226 eV., are shown by the
dashed curve in figure 30. The results of the two experi-
ments are normalized to each other at 0.11 eV. There is
qualitative agreement between the two sets of results in
that both show a rapidly increasing cross section with
increasing energy from an apparent low energy threshold to
a maximum. However, there is   quantitative disagreement
between the results at low energies. The TOF results predict
a threshold at approximately 0.01 eV. The present results
indicate that the threshold will be at approximately 0.05 eV.
if the cross section continues to drop rapidly at the lower
energies. Also, the results of the present study indicate
that the cross section decreases gradually at higher energies.

There are several possible explanations for these
discrepancies. The metastable argon atom source for the

128

TOF method is an electron impact source utilizing 20 volt electrons. The $^3P_2/^3P_0$ ratio for this source is not known. This ratio for the present study is expected to be nearly the same (7/1) as in Tang's source,[60] although there may be some difference due to the significantly higher discharge currents employed in this work. Different percentages of the two components could have a large effect on the energy threshold. The energy difference, $^3P_0$ (11.72 eV.) - $^3P_2$ (11.55 eV.), is 0.17 eV. From the curve crossing model which has been proposed for this reaction, it might be expected that the $^3P_0$ state will produce a cross section curve with a lower threshold energy than a similar curve for the $^3P_2$ state.

The target beam source for the TOF measurements is an effusive source cooled to $80°K$ for the low energy studies. The nitrogen nozzle beam of this study is significantly "cooler" rotationally (see section IIIC). As much as 0.007 eV. more rotational energy is available in the TOF experiments at low energies. Another characteristic of nozzle beams, partial alignment of the molecules with their angular momenta preferentially oriented at right angles to the beam direction,[103] is not found in the effusive beam of the TOF study.

The wavelength response of the detection systems was nearly the same at the low wavelength end. Above 3800 $\overset{\circ}{A}$ a bandpass filter used in the TOF experiment greatly reduces

the detection efficiency. From Table VII it is seen that the most important transitions are below 3800 Å. Since the wavelength response becomes important only if the relative vibrational level populations change with collision energy, it is not likely that significant differences in the results of the two studies could be caused by this factor (see section IVA).

Consideration should be given to the energy resolutions of the two experiments. The TOF resolution is worst at the lowest energy (0.013 eV.) where $w(E_r) = 0.33$. This resolution is defined in terms of the standard deviation and should be multiplied by 2.3 for comparison with the resolution of this study, given in terms of the half-width. At 0.013 eV. the energy resolution of the TOF results is 0.76 which gives an energy spread of 0.008 eV. Though the energy spread will make the apparent threshold appear at lower energy than the actual threshold, it does not account for the 0.04 eV. threshold difference observed. At the lowest relative collision energy (0.06 eV.) of this study, the energy resolution is 0.34. For comparison, the energy resolution of the TOF experiment is about 0.46 at this energy.

Of the experimental conditions discussed above, it seems that the different source conditions, particularly the metastable atom beam source conditions, offer the most likely explanation for the low energy disagreement between the time-of-flight results and the present results. Current

studies which promise to shed light on some of the aspects just mentioned, will be discussed in section VID.

Other studies of the Ar^*/N_2 system have been measurements of total quenching cross sections at a single energy under conditions of poor resolution. The flowing afterglow rate constants[35], 3.6×10^{-11} cm^3 sec.$^{-1}$($^3P_2$) and 1.6×10^{-11} cm^3 sec.$^{-1}$($^3P_0$), were measured at room temperature with the relative energy distribution shown in figure 34. The average energy for the 300^OK distribution is 0.033 eV. The cross sections, 5.8 $\overset{O}{A}^2$($^3P_2$) and 2.5 ($^3P_0$), presented in Table II of reference 35 were calculated from equation (11). Given the strong relative velocity dependence of the cross section at low relative velocities, this procedure is not expected to yield accurate cross sections.

Winicur and Fraites[21] have measured differential scattering cross sections for $Ar(^3P_{2,0}) + N_2$ using a metastable atom source with unspecified $^3P_2/^3P_0$ ratio. By assuming that small angle scattering is purely elastic, they calculated a five parameter double-Lennard-Jones potential, and used this to calculate elastic scattering cross sections at large angles. The difference in the calculated elastic cross sections and the measured cross sections at large angles was attributed to inelastic scattering. By subtracting the experimentally measured differential cross sections from the calculated elastic scattering cross sections they calculated the probabilities $P(b)$ for energy

Figure 34. Ar/N_2 Relative Velocity Distributions Maxwell-Boltzmann Distributions at

■ 77°K

● 300°K
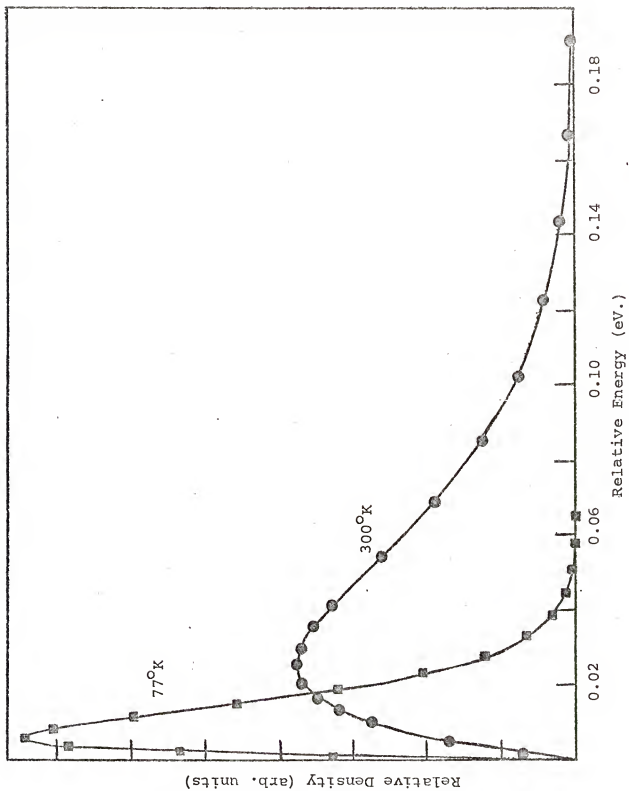
exchange as a function of impact parameter b. By integrating
P(b) over the impact parameter, they obtained an integral
cross section for energy exchange of 11.8 $\overset{\circ}{A}^2$ at 0.051 eV.
This corresponds to a cross section for production of $N_2(C)$
and $N_2(B)$ since no other states appear to be directly popu-
lated. The energy resolution $\frac{\Delta E}{E}$ was 1.5 so that $\Delta E = 0.08$ eV.
From the value of the potential energy at $P(b) = 0$, the
threshold energy was estimated to be 0.008 eV. The effect
of the poor energy resolution on this calculated threshold
energy was not discussed, but the effect on the integral
cross section is clear. The cross section at 0.051 eV. is
enhanced by the larger cross sections from relative energies
as high as 0.09 eV. and reduced by the lower cross sections
from energies as low as 0.01 eV.

If the threshold energy of 0.008 eV. is correct, then
the threshold for production of $N_2(B)$ plus $N_2(C)$ is the
same as the threshold for production of $N_2(C)$ measured by
Lee and Martin. Also, if the intermediate complex mechanism
suggested by Stedman and Setser[10] (see section IE) is correct,
the TOF results imply that the observed threshold energy is
a barrier to formation of a complex which subsequently dis-
sociates to $N_2(C)$ and $N_2(B)$. However, the results (reference
21) on which this conclusion is based, also present strong
evidence that the Ar*/N_2 interaction does not involve complex
formation; that is, the differential scattering experiments
showed pronounced backward scattering indicative of a direct

mechanism. In addition, any conclusion based on the thresholds for production of $N_2(C)$ and $N_2(B)$ in these experiments assumes that the threshold energies are not effected by the different $^3P_2/^3P_0$ ratios for the metastable atom beams used.

Stronger evidence that the cross sections for production of $N_2(C)$ and $N_2(B)$ behave similarly at low relative energies comes from flowing afterglow studies[104] at 300°K and 77°K. The relative population of $N_2(C)$ to $N_2(B)$ was the same at both temperatures. Consideration of figure 34 shows that, if the threshold energies for producing $N_2(C)$ and $N_2(B)$ were 0.05 eV. and 0.01 eV., respectively, the relative population $N_2(C)/N_2(B)$ would increase greatly in going from 77°K to 300°K. Since this does not occur, the low energy behavior of the cross sections for $N_2(C)$ and $N_2(B)$ production appear to be similar. This assumption, plus the assumption that the total quenching cross section has a threshold of 0.01 eV., suggests that the most likely explanation for the higher threshold observed in this study is that it corresponds $^3P_2$ interactions of argon with N_2. The lower threshold would then be due to $^3P_0$ interactions only.

B. Ar*/N_2 - Reaction Mechanism

The following information from various techniques discussed in Chapter I has been obtained concerning interactions of argon metastable atoms with ground state nitrogen molecules:

1) Only the $N_2(B)$ and $N_2(C)$ states are populated directly and the ratio $N_2(B)/N_2(C)$ for the initial products formed is 6 ± 1. This ratio is independent of temperature.[97]

2) The vibrational energy levels of $N_2(C)$ are not populated according to the Franck-Condon factors for transitions between ground state N_2 and the vibrational levels of $N_2(C)$. In particular, the $v' = 0$ level of $N_2(C)$ is much more heavily populated than would be expected for a Franck-Condon transition, and only the $v' = 0$, 1, and 2 levels are populated.[96]

3) The lower $N_2(B)$ vibrational levels are the most highly populated.[97]

4) Considerable rotational excitation accompanies the formation of $N_2(C)$, and intensity alternations between even and odd rotational levels were observed.[97]

5) The relative vibrational level populations of $N_2(C)$ are independent of temperature.[96]

6) Differential scattering measurements[21] show predominantly backward scattering of Ar* by N_2.

7) The cross section for production of $N_2(C)$ in collisions with $Ar(^3P_{2,0})$ rises rapidly from an apparent threshold to a maximum at about 0.1 eV.

Observations 2) and 4) are indicative of very strong interaction between metastable argon and nitrogen. This is in contrast with weak interactions observed in the Penning ionization reaction discussed in the next section.

Observation 1) is consistent with the formation of $N_2(B)$ and $N_2(C)$ in the same dynamic process. This led to the proposal of a reaction which proceeds via an intermediate complex which dissociates to $N_2(B)$ and $N_2(C)$ (see section IIE). This mechanism explains observations 1) - 5), but directly contradicts observation 6) and fails to explain the existence of a threshold energy which was observed in this study and in reference 22. This electron exchange mechanism is unacceptable for other reasons mentioned in reference 35.

The energy dependence of the cross section shown in figure 30 suggests that the reaction proceeds through a curve crossing mechanism. In this model, depicted in figure 35A, only transitions which occur near the crossing point R_0 are probable. The threshold energy corresponds to the relative translational energy ΔE needed to reach the curve crossing. By varying the parameters R_0, α and β of equation (22), several Landau-Zener cross section curves were calculated. One such curve, parameterized to agree at the maximum, is shown in figure 30. None of the calculated curves could be made to fit either the present results or those of reference 22. Since the treatment is valid only for single curve crossings in atom-atom collisions, this disagreement is not really surprising. Transitions from $N_2(X)$ occur to three different vibrational states and many
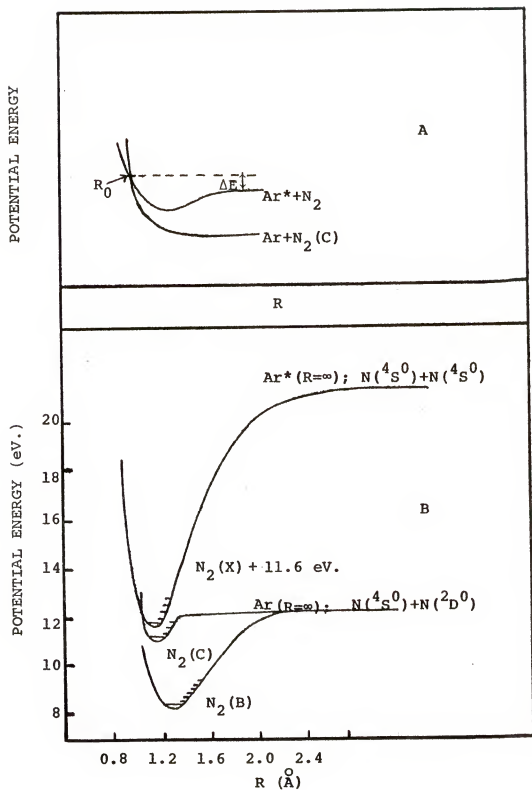
Figure 35. Curve Crossing Diagrams

different rotational states of $N_2(C)$, leading to many potential curve crossings instead of the one shown in figure 35A.

Another type of curve crossing is demonstrated in figure 35B. The curves shown are the $N(^4S^0) + N(^4S^0)$ interaction potential curve leading to $N_2(X)$ with Ar* at $R = \infty$, and two of the N_2 excited state potential curves with $Ar(^1S)$ at $R = \infty$. As Ar* approaches the N_2 molecule, the curves shown would drop to lower potential energies due to strong interaction, and overlap of the entrance and exit channels occurs. The relative vibrational level populations of $N_2(C)$ and $N_2(B)$ which result depends on the relative positions of the two curves at the instant of the transition. Such a picture might explain why $v' = 0$ of $N_2(C)$ is favored over $v' = 1$ and 2 despite the fact that the latter states are closer to being resonant with Ar* + $N_2(X)$.

C. $\underline{He^*/N_2}$

Results from Penning electron spectroscopy[18b] have established several characteristics of Penning ionization[105] of N_2 in collisions with He*. These are summarized below:

1) Three electronic states are produced – $N_2^+(X)$, $N_2^+(A)$, and $N_2^+(B)$ in relative populations of 0.35, 0.24, and 0.41, respectively, at 300-$400°K$.

2) The vibrational levels of each electronic state are populated according to the Franck-Condon factors for

transitions between the vibrational levels of the ion and the isolated ground state molecule.

3) Only a small amount of energy δ is converted from relative translational motion of the nuclei into kinetic energy of the ejected electron. This value of δ is independent of which electronic state is formed.

4) The Penning electron energy distributions are narrow compared to the distributions for He*/Hg, Na, K.

Observations 2), 3), and 4) are strong evidence that neither the interaction of He* with N_2 nor He with N_2^+ is very strong. The potential curves which describe the collision have shallow well depths and collision energy is converted to electron energy near the classical turning point.[18c] The distance between helium and nitrogen is large compared to the nitrogen molecule equilibrium distance, so that application of the theory of metastable atom-atom collisions (section IID) to metastable helium-nitrogen collisions is justified.

Use of equations (6), (16), and (21) of Chapter I requires expressions for $V[He*-N_2]$ and $\Gamma(R)$. Illenberger and Niehaus[16] and Olson[106] have performed calculations for the He(2^3S)/Ar system by using an analytical function for $V(He*-Ar)$ which agrees with a potential determined from scattering data by Chen et al.[107] Accurate potential functions for He*/N_2 are not yet available from scattering data. By analogy with He*/Ar and Li/Ar potentials[108,109]

it is expected that a reasonable potential function could be constructed for He*/N_2. In fact, recent scattering experiments[110] indicate that the long range interaction of He* - N_2 is almost identical to Li - N_2.

The He(2^3S)/Ar calculations of reference 16 employed the parametrized function, a exp(-R/b), for Γ reflecting the expectation that values of R closest to the classical turning point are favored. The parameters a and b were adjusted by comparison with the absolute values and general shape of the experimentally determined cross section curve.

Illenberger and Niehaus[16] have shown that the parameter b may be estimated from portions of the measured cross section curve. In the regions where the collision energy is much greater that the well depth of the interaction potential and the ionization efficiency is much less than unity, b may be determined from the slope k of the cross section curve by

$$\frac{1}{2}(k+1) \approx D/b \qquad (30)$$

where D may be determined from the repulsive part of the interaction potential V(R) = C exp(-R/D). It was also shown that the ratio of the well depth of the interaction potential to the minimum in the cross section curve is very sensitive to b.

Since D is the same for total ionization as for ionization to N_2^+(B), and since k is larger for total ionization, then, b is smaller for total ionization. The ratio Γ_B/Γ_T of

the B state coupling width to the total ionization coupling width is given by

$$\frac{\Gamma_B}{\Gamma_T} = \frac{a_B}{a_T} \exp \left[\frac{1}{b_T} - \frac{1}{b_B}\right] R$$

where the subscripts T and B refer to total ionization and ionization to the B state, respectively. For $b_T < b_B$, Γ_B/Γ_T increases with increasing R. Therefore, the present results indicate that the B state is favored for low energy collisions in which transitions occur at relatively large values of R.

A complete theoretical analysis has not been carried out at this time since accurate potential functions are forthcoming from the results of reference 110, and theoretical calculations for total ionization of N_2 by He^* are expected from the results of reference 16.

D. Summary

The qualitative nature of the $Ar^*/N_2(C)$ cross section curve (figure 30) is further evidence of a curve crossing mechanism. Quantitative discrepancies between these results and those from the time-of-flight study are important for illuminating certain details of the reaction mechanism as discussed in section VIA. These discrepancies may be resolved as data becomes available from other studies. For instance, measurements being made in this laboratory will determine whether differences in wavelength response of the

detection systems employed are important by determining the translational energy dependence of relative $N_2(C)$ vibrational level populations. Selective removal of either singlets or triplets in a neon metastable atom beam has been accomplished with a tunable dye laser and used to measure the $^3P_2/^3P_0$ ratio for an electron impact source operated at various electron energies.[111] Application of this technique to Ar* would be very useful in deciding whether the difference in the $^3P_2/^3P_0$ ratio in electron impact and discharge sources explains the differences in the measured cross sections near threshold.

The results of cross section measurements for He*/N_2 indicate that $N_2^+(B)$ is favored at low energies due to a smaller R dependence of the coupling width compared to that dependence for the other electronic states formed. If $N_2^+(A)$ is also favored at low energies, as qualitatively observed (section IVB), the fraction of $N_2^+(X)$ produced must increase with increasing collision energy.

APPENDIX I: I → V CONVERTER/AMPLIFIER

The circuit shown in figure 36 was designed to convert current pulses from the electron multiplier (EM) anode into voltage pulses of suitable magnitude for nozzle beam intensity and time-of-flight analyses. The first stage is an I → V converter with a $10^5 \Omega$ feedback resistor. The output voltage $V_0(1)$ of this stage is given by $V_0(1) = (10^5)(I_{in})$. This output is proportional to the nozzle beam intensity and is measured by a lock-in amplifier. The second stage is a non-inverting operational amplifier. Depending on the position of switch S2, a gain of either 100 or 1000 is possible. The electron multiplier anode currents are such that the gain of 1000 is needed for a satisfactory waveform eductor input. The capacitors across the feedback resistors serve to smooth the pulses. By closing switch S2, a current may be supplied to suppress the D.C. background if desired.

The response time of this circuit is less than two μsec. so that effects on the measured flight times are negligible.
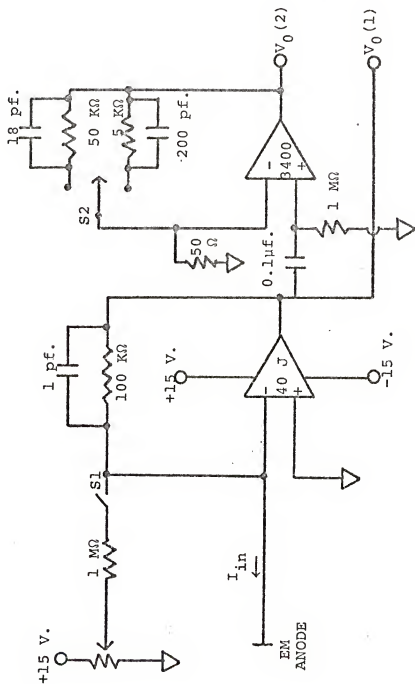
Figure 36. I → V Converter/amplifier

APPENDIX II: PULSE SHAPING CIRCUIT FOR FREQUENCY COUNTER

The signal from an LS-400 photo transistor is formed
(stage A), shaped (stage B), and made TTL compatible
(stage C) by the circuit shown in figure 37. Stage B is a
Schmitt Trigger which converts the relatively slow rising
pulses from the velocity selector LS-400 into sharp pulses,
and stage C interfaces the Schmitt Trigger to the 7400 gate
of the frequency counter.

A similar circuit is used to shape pulses from the
nozzle beam chopper. However, greater sensitivity was
achieved by applying the photo transistor signal directly to
the base of the 2N5134 transistor. The additional sensitivity
allowed reduction of the light emitting diode intensity
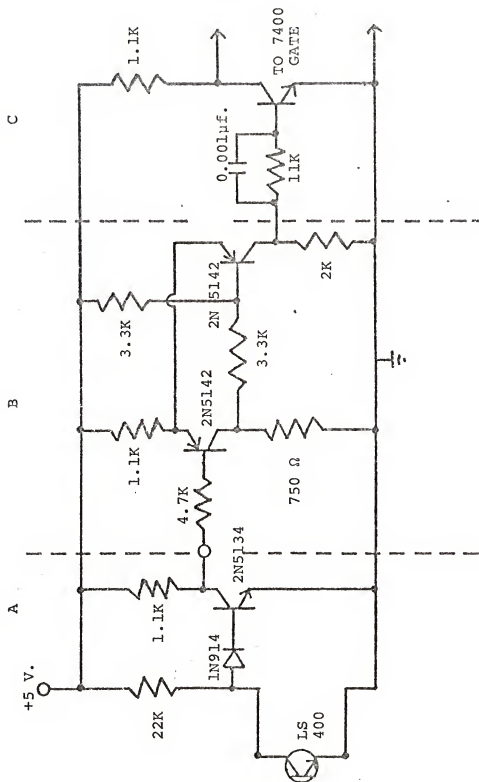and consequent reduction of the bias discussed in section IVC.

Figure 37. Pulse Shaping Circuit

APPENDIX III: PULSE SEPARATOR

The pulses from an LS-400 photo transistor mounted on the nozzle beam chopper are shaped by a Schmitt Trigger circuit (see Appendix II). It is necessary to separate the alternating long and short pulses into separate pulse trains in order to trigger the lock-in amplifier and waveform eductor properly. This separation is accomplished by the logic circuit shown in figure 38.

The flip-flop changes state with the decay of each pulse, sending alternate pulses to different outputs. The purpose of the "one-shots" (OS 1 and OS 2) is to insure that the short pulses always appear at output 1 and the long pulses at output 2. By proper choice of OS 1 and OS 2, the 7400 NAND gate will re-set the flip-flop if the initial pulse appears at the wrong output.
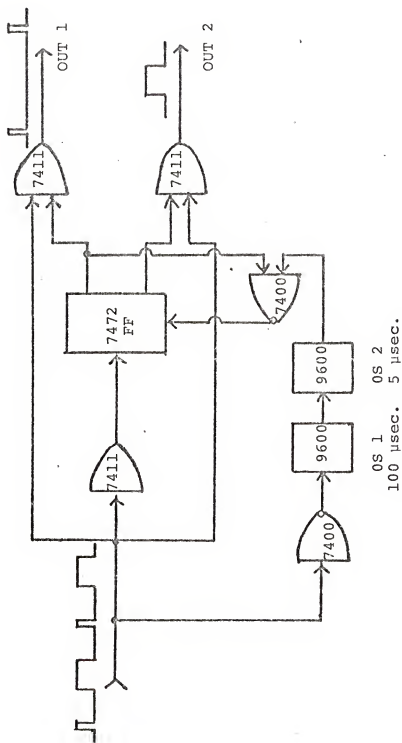
Figure 38. Pulse Separator

REFERENCES

1. K. J. Laidler, "The Chemical Kinetics of Excited States," Oxford University Press, Amen House, London, 1955, p. 87.

2. R. D. Levine and R. B. Bernstein, "Molecular Reaction Dynamics," Oxford University Press, New York, 1974, p. 169.

3. M. J. Rees, D. W. Sciama, and S. H. Stobbs, _Astrophys._ _Lett._, _2_, 243, 1968.

4. C. K. N. Patel, "Lasers," Vol. 2, A. K. Levine, ed., E. Arnold and Co., London, 1968.

5. R. D. Levine and R. B. Bernstein, "Molecular Reaction Dynamics," Oxford University Press, New York, 1974, p. 122.

6. A. A. Kruithoff and F. M. Penning, _Physica_, _4_, 430, 1937.

7. R. H. Garstang, in D. R. Bates, ed., "Atomic and Molecular Processes," Academic Press, New York, 1962, Chapter 1.

8. G. Cario and J. Franck, _Z. Physik_, _17_, 202, 1923.

9. E. J. B. Willey, "Collisions of the Second Kind," E. Arnold and Co., London, 1937.

10. D. H. Stedman and D. W. Setser, in G. Porter, ed., "Progress in Reaction Kinetics," _6_, 193, Pergamon Press, New York, 1971.

11. A Fontijn, in G. Porter, ed., "Progress in Reaction Kinetics," _6_, 75, Pergamon Press, New York, 1971.

12. F. W. Lampe, in J. Franklin, ed., "Ion-Molecule Reactions," 601, Plenum Press, New York, 1972.

13. R. D. Rundel and R. L. Stebbings, in M. R. C. McDowell and E. W. McDaniel, eds., "Case Studies in Atomic Collision Physics," _2_, 547, North-Holland, Amsterdam, 1972.

14. S. Y. Tang, A. B. Marcus, and E. E. Muschlitz, Jr., _J. Chem. Phys._, _56_, 566, 1971.

15. A. Pesnelle, H. Haurdin, G. Watel, and C. Manus, J. Phys., B6, L326, 1973.

16. E. Illenberger and A. Niehaus, to be published in Z. Physik.

17. (a). V. Cermák, Collect. Czech. Chem. Commun., 33, 2739, 1968.

    (b). V. Cermák and J. B. Ozenne, Int. J. Mass. Spectrom. and Ion Phys., 7, 399, 1971.

18. (a). H. Hotop and A. Niehaus, Z. Physik, 215, 395, 1968.

    (b). H. Hotop and A. Niehaus, Int. J. Mass Spectrom. and Ion Phys., 5, 415, 1970.

    (c). H. Hotop and A. Niehaus, Z. Physik, 228, 68, 1969.

    (d). H. Hotop and A. Niehaus, ibid., 238, 452, 1970.

19. E. E. Ferguson, F. L. Fehsenfeld, and A. L. Schmeltekopf, in D. R. Bates, ed., "Advances in Atomic and Molecular Physics," V, Academic Press, New York, N.Y., 1970.

20. R. C. Bolden, R. S. Hemsworth, M. J. Shaw, and N. D. Twiddy, J. Phys., B: Atom. Molec. Phys., 3, 45, 61, 1970.

21. D. H. Winicur and J. L. Fraites, J. Chem Phys., 61, 1548, 1974.

22. W. Lee and R. M. Martin, J. Chem. Phys., 63, 962, 1975.

23. E. E. Ferguson, Phys. Rev., 128, 210, 1962.

24. D. R. Bates, K. L. Bell, and A. E. Kingston, Proc. Phys. Soc., 91, 288, 1967.

25. J. R. Penton and E. E. Muschlitz, Jr., J. Chem. Phys. 49, 5083, 1968.

26. See reference 18b, p. 438.

27. A. Niehaus, Tenth International Conference on Phenomena of Ionized Gases, Oxford, England, 1971. The description in reference 10 follows this presentation by Dr. Niehaus.

28. See reference 10, p. 218.

29. H. Nakamura, J. Phys. Soc. Japan, 26, 1473, 1969.

30. W. H. Miller, J. Chem. Phys., 52, 3563, 1970.

31. C. H. Chen, H. Haberland, and Y. T. Lee, J. Chem. Phys., 61, 3095, 1974.

32. W. C. Richardson and D. W. Setser, J. Chem. Phys., 58 1809, 1973.

33. See reference 18b, p. 439.

34. D. R. Herschbach, in J. Ross, ed., "Ad. Chem. Phys.," X, 367, Interscience, New York, N.Y., 1966.

35. L. G. Piper, J. E. Velazco, and D. W. Setser, J. Chem. Phys., 59, 3323, 1973.

36. See reference 21, pp. 1551, 1552.

37. S. Geltman, "Topics in Atomic Collision Theory," Academic Press, New York, p. 213, 1969.

38. C. Zener, Proc. Roy. Soc., A137, 696, 1932, for example.

39. E. Fink and K. H. Welge, Z. Naturforsch, 19a, 1193, 1964.

40. J. E. Hesser, J. Chem.Phys., 48, 2518, 1968.

41. A. L. Schmeltekopf and F. C. Fehsenfeld, J. Chem. Phys., 53, 3173, 1970.

42. Airco Industrial Gases, Murray Hill, N. J. 07074. Helium, argon, and nitrogen used were rated at better than 99.995% purity.

43. Wallace and Tiernan Division, Pennwalt Corporation, Belleville, N. J.; model FA 160

    (a) Serial number: UU 15101, range: 0.1 - 20 torr.

    (b) Serial number: TT 15101, range: 0 - 30 PSI.

44. Speedivac, Edwards High Vacuum, LTD., Manor Royal, Crawley, Sussex. Model 8 - 1, range: 10^{-3} - 10 torr.

45. Cenco, Hyvac 2, Central Scientific Co., Chicago, Ill., Serial number: 1506.

46. Teledyne - Hastings - Raydist, Hampton, Va. Model ALL-100P, range: 0 - 100 SCCM for helium. Model ALL-50P, range: 0 - 50 SCCM for nitrogen.

47. Nupro Company, Cleveland, Ohio.

48. Consolidated Vacuum Corp., Rochester, New York.

   (a)   Type GTC - 100

   (b)   Model B, 10"; maximum pumping speed in air:
         2500 ℓ/sec.

49. NRC Operation, Varian Vacuum Div., Newton, Massachusetts.

   (a)   Model VHS - 4; maximum pumping speed for air:
         1200 ℓ/sec.

   (b)   Model VHS - 6; maximum pumping speed for air:
         2400 ℓ/sec. (1600 ℓ/sec. with "hat cap").

   (c)   NRC 836 Vacuum Ionization Gauge, thermocouple
         gauges for nozzle and discharge forelines,
         ionization gauge controller for nozzle chamber
         ionization gauge.

50. Sargent-Welch Scientific Company, Skokie, Ill. Welch
     "Duo Seal" Vacuum Pumps.

   (a)   Model 1402, 5.6 CFM.

   (b)   Model 1375, 35 CFM.

   (c)   Model 1397, 18 CFM.

51. Ultek Corporation, Palo Alto, Cal., Model 50-003.

52. Veeco Instruments Inc., Plainview, N.Y.

   (a)   Type RG75K; nozzle chamber ionization gauge is
         controlled by NRC 836 controller (reference 49c).
         Discharge and main chamber gauges are controlled
         by Veeco RG-21X Vacuum Gauges.

   (b)   Vacuum Controller TC9.

53. Bendix Scientific Instruments and Equipment, Rochester,
     N.Y., Type BC-016.

54. Edwards High Vacuum Inc., Grand Island, N.Y., Flowtrol
     Type F.S.1.

55. S. Y. Tang, Velocity Dependence of the Ionization of
     Gas Molecules on Impact of Metastable Atoms, Ph.D.
     Dissertation, University of Florida, p. 20, 1970.

56. E. E. Muschlitz, Jr., H. D. Randolph, and J. N. Ratti,
     Rev. Sci. Insr., 33, 446, 1962.

57. Lambda Electronics Corp., Huntington, N.Y., model
     LE 101-FM.

58. Trygon Electronics, Inc., Roosevelt, N.Y., model M36-30A.

59. Sorenson Power Supplies, Raytheon Co., Manchester, N.H., model DCR150-2.5A.

60. See reference 55, p. 66.

61. A. V. Phelps, Phys. Rev., 99, 1307, 1955.

62. R. Grice, Alkali Atom Reactive Scattering and the Electron-Jump Model, Ph.D. thesis, Harvard University, 1968.

63. J. L. Kinsey, Rev. Sci. Instr., 37, 61, 1966.

64. Globe Industries of TRW Inc., Dayton, Ohio.

    (a) Part number 75A1003-2.

    (b) Part number 53A118-2.

65. California Instruments Corp., San Diego, Cal.

    (a) Series 800T-20/20 Khz.

    (b) Invertron Model 101T.

66. (a) Original bearings were GRW 714A, Globe number 15 D034 A066-9D 1308-3.

    (b) The Barden Corporation, Danbury, Conn., Barden Bartemp bearings, SR4SSTB.

67. See reference 55, p. 23.

68. Ball Brothers Research Corporation, Boulder, Colo. VKX-4-DP-XXG.

69. Texas Instruments, Inc., Dallas, Texas, type TIL 31, p-n gallium arsenide light source.

70. Photocell is an LS 400, n-p-n planar silicon photo transistor.

71. H. U. Hostettler and R. B. Bernstein, Rev. Sci. Instr., 31, 872, 1960.

72. See reference 55, pp. 49-54.

73. Keithley Instruments, Inc., Cleveland, Ohio, model 603 electrometer amplifier.

74. Bendix Corp., Cincinnati Div., Cincinnati, Ohio, model 306 magnetic electron multiplier, current gain: 10^7.

75. (a) J. B. Anderson and J. B. Fenn, _Phys Fluids_,
        _8_, 780, 1965.

    (b) J. B. Anderson, R. P. Andres, and J. B. Fenn, in
        J. Ross, ed., "Ad. Chem. Phys.," X, 275,
        Interscience, New York, N.Y., 1966.

    (c) H. Ashkenhas and F. S. Sherman, in J. H. de Leeuw,
        ed., "Rarefied Gas Dynamics," _2_, Academic Press,
        New York, N.Y., 1966.

76. The basic design of the nozzle and skimmer is due to
    O. Hagena, J. Scott, Jr., and A. Varma, University of
    Virginia Technical Report No. AST-4038-103-67u, 1967,
    p. 9.

77. J. P. Toennies, in W. Jost, ed., "Physical Chemistry,
    an Advanced Treatise," _VI_ _A_, 227, Academic Press,
    New York, N.Y., 1974.

78. See reference 75a, p. 784.

79. Krohn-Hite Corp., Cambridge, Mass.

    (a) Model 440A(R).

    (b) Model DCA-10(R).

80. Electronic Associates, Inc., Palo Alto, Cal.

    (a) Quad 210, range: 1-500 a.m.u., resolution on
        low range: 2 × mass number.

    (b) 14 stage, Cu-Be dynodes, gain: 10^6 before
        contamination.

81. Princeton Applied Research, Princeton, N.J.

    (a) Model 121 lock-in amplifier/phase detector.

    (b) Model TDH-8 waveform eductor.

82. Hewlett-Packard Company, Palo Alto, Cal.

    (a) Model 140A.

    (b) Model 214A.

83. Rolyn Optics Co., Arcadia, Cal.

    (a) Stock No. 17.1200, 68 mm diameter, 38.1 mm focal
        length.

(b) Stock No. 61.2150, 50 mm diameter, 17.0 mm focal length.

(c) Stock No. 65.1330.

84. EMI, Gencom Div., Plainview, N.Y., model 9558 with extended S-20 cathode.

85. Products for Research, Inc., Danvers, Mass., model TE-104 TS-RF.

86. Northeast Scientific Co., Acton, Mass., model RE-5006, 5 kV.

87. SSR Instruments Co., Santa Monica, Cal.

(a) Model 1120 amplifier/discriminator.

(b) Model 1110 digital synchronous computer.

88. Leeds and Northrup, Philadelphia, Pa., Speedomax G.

89. United Systems Corp., Dayton, Ohio.

(a) Model 266.

(b) Datos 305 Data Coupler.

90. Teletype Corporation, Skokie, Ill.

91. Spex Industries, Inc., Metuchen, N.J.

92. F. B. Dunning and A. C. H. Smith, J. Phys. B: Atom. Molec. Phys., 4, 1696, 1971.

93. Computer Designs Corporation, Los Angeles, Cal., Compucorp model 425G.

94. T. R. Govers, R. L. LeRoy, and J. M. Dickers, in L. Trilling and H. Y. Wachman, eds., "Rarefied Gas Dynamics," Sixth Symposium, 985, Academic Press, New York, N.Y., 1969.

95. J. P. Toennies, Lectures at the University of Florida, February, March, 1975.

96. D. H. Stedman and D. W. Steser, J. Chem. Phys., 52 3957, 1970.

97. D. W. Setser, D. H. Stedman, and J. A. Coxon, 53, 1004, 1970.

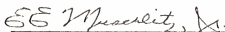98. F. R. Gilmore, J. Quant. Spectry. Radiative Transfer, 5, 369, 1965.

99. M. Jeunehomme and A. B. F. Duncan, _J. Chem. Phys._, __41__, 1692, 1964.

100. Optical Industries, Inc., Costa Mesa, Cal., stock no. 03 FIA 001.

101. R. W. Nicholls, _Journal of Research of the National Bureau of Standards- A. Physics and Chemistry_, __65A__, 451, 1961.

102. See reference 32, p. 1813.

103. M. P. Sinha, C. D. Caldwell, and R. N. Zare, _J. Chem. Phys._, __61__, 491, 1974.

104. See reference 97, p. 1010.

105. Associative ionization has not been observed for He^*/N_2.

106. R. E. Olson, _Phys. Rev._, __A6__, 1031, 1972.

107. See reference 31, p. 3098.

108. See reference 31, p. 3095.

109. G. B. Ury and L. Wharton, _J. Chem. Phys._, __56__, 5832, 1972.

110. S. M. Trujillo, in J. S. Risley and R. Geballe, eds., "Electronic and Atomic Collisions," __1__, 437, University of Washington Press, Seattle, Wash., 1975.

111. T. B. Cook, W. P. West, F. B. Dunning, and R. F. Stebbings, in J. S. Risley and R. Geballe, eds., "Electronic and Atomic Collisions," __2__, 966, University of Washington Press, Seattle, Wash., 1975.

BIOGRAPHICAL SKETCH

Robert Alan Sanders was born September 7, 1949 in Johnson City, Tennessee. He graduated from Science Hill High School in Johnson City in 1967. He attended Davidson College from 1967-1969 and graduated with a Bachelor of Arts degree in Chemistry from Vanderbilt University in 1971. From 1971 to 1973, he completed requirements for a Master of Science degree in physical chemistry at the University of Florida. From 1973 to present, he has pursued studies in chemistry leading to the degree of Doctor of Philosophy.

He is married to the former Lee Knisley who is completing Ph.D. requirements in Mathematics concurrently.

I certify that I have read this study and that in my opinion it conforms to acceptable standards of scholarly presentation and is fully adequate, in scope and quality, as a dissertation for the degree of Doctor of Philosophy.
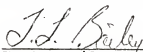
E. E. Muschlitz, Jr., Chairman
Professor of Chemistry

I certify that I have read this study and that in my opinion it conforms to acceptable standards of scholarly presentation and is fully adequate, in scope and quality, as a dissertation for the degree of Doctor of Philosophy.

S. O. Colgate
Professor of Chemistry

I certify that I have read this study and that in my opinion it conforms to acceptable standards of scholarly presentation and is fully adequate, in scope and quality, as a dissertation for the degree of Doctor of Philosophy.

T. L. Bailey
Professor of Physics

This dissertation was submitted to the Graduate Faculty of the Department of Chemistry in the College of Arts and Sciences and to the Graduate Council, and was accepted as partial fulfillment of the requirements for the degree of Doctor of Philosophy.

August, 1975

Dean, Graduate School